Comput. Methods Appl. Mech. Engrg. 267 (2013) 400–417

Contents lists available at ScienceDirect

Comput. Methods Appl. Mech. Engrg.

journal homepage: www.elsevier.com/locate/cma

Energy stable flux reconstruction schemes for advection–diffusion problems

P. Castonguay [a,*], D.M. Williams [a], P.E. Vincent [b], A. Jameson [a]

[a] Department of Aeronautics and Astronautics, Stanford University, Stanford, CA 94305, USA
[b] Department of Aeronautics, Imperial College London, South Kensington, London SW7 2AZ, UK

ARTICLE INFO

Article history:
Received 20 December 2012
Received in revised form 1 July 2013
Accepted 20 August 2013
Available online 30 August 2013

Keywords:
High-order
Unstructured
Discontinuous Galerkin
Spectral difference
Flux reconstruction
Diffusion

ABSTRACT

High-order methods for unstructured grids provide a promising option for solving challenging problems in computational fluid dynamics. Flux reconstruction (FR) is a framework which unifies a number of these high-order methods, such as the spectral difference (SD) and collocation-based nodal discontinuous Galerkin (DG) methods, allowing for their more concise and flexible implementation. Additionally, the FR approach can be used to facilitate development of new numerical methods that offer arbitrary orders of accuracy on unstructured grids. In previous work, it has been shown that a particular range of FR schemes, referred to as Vincent–Castonguay–Jameson–Huynh (VCJH) schemes, are guaranteed to be stable for linear advection problems for all orders of accuracy. There have remained questions, however, regarding the stability of FR schemes for advection–diffusion problems. In this study a new class of VCJH schemes is developed for solving one-dimensional advection–diffusion problems. For the first time, it is shown that the schemes are linearly stable for linear advection–diffusion problems for all orders of accuracy on nonuniform grids. Linear and nonlinear numerical experiments are performed in 1D and 2D to investigate the accuracy and stability properties of the new schemes. The results indicate that certain VCJH schemes for advection–diffusion problems possess significantly higher explicit time-step limits than discontinuous Galerkin schemes, while still maintaining the expected order of accuracy.

1. Introduction

Recent years have seen significant interest in the development of high-order methods for solving conservation laws. High-order methods produce less numerical dissipation relative to their lower order counterparts, allowing them to better resolve temporally evolving physical features. For example, in the context of fluid dynamics, high-order methods are known for their superior ability to preserve propagating vortex structures when simulating flows around rotorcraft, turbo-machinery, and flapping wings [1]. In addition, high-order methods perform more efficiently on problems with low error tolerances [2]. They have been successfully employed to simulate low-amplitude waves for applications in the areas of aeroacoustics and magnetohydrodynamics [3]. However, despite their advantages, high-order methods have yet to be adopted by the majority of fluid dynamicists. Instead, low order methods are more popular in industrial settings because they are more robust and easier to implement on the unstructured meshes which are frequently employed within complex geometries in

* Corresponding author. Tel.: +1 650 336 4880; fax: +1 650 723 3018.
E-mail addresses: pcasto2@alumni.stanford.edu (P. Castonguay), davidmw@alumni.stanford.edu (D.M. Williams), p.vincent@imperial.ac.uk (P.E. Vincent), jameson@baboon.stanford.edu (A. Jameson).

0045-7825/$ - see front matter © 2013 Elsevier B.V. All rights reserved.
http://dx.doi.org/10.1016/j.cma.2013.08.012

practical applications. In order to remedy this situation, significant efforts have been devoted towards developing high order methods that are well-suited for unstructured grids.

The discontinuous Galerkin (DG) methods are perhaps the most well-known amongst high-order methods for unstructured grids. Traditional DG methods [4] have been successfully applied to the treatment of nonlinear conservation laws including the Euler and Navier–Stokes equations [5–7]. Recently, a nodal approach (referred to as collocation-based nodal DG) has gained popularity [2]. This approach is easier to implement than the (aforementioned) traditional DG methods as it is 'quadrature free' in the sense that it omits the explicit quadrature procedures associated with the traditional DG methods. In addition, the spectral difference (SD) approach, which was originally proposed in 1996 by Kopriva and Kolias [8], has gained popularity as a quadrature free method. This method was generalized in 2006 by Liu, Vinokur, and Wang [9], and has thereafter been successfully applied to a wide assortment of problems on unstructured grids [10–13].

Flux reconstruction (FR) emerged in 2007 as a single framework which encompasses a variety of collocation-based nodal DG and SD approaches. Originally proposed by Huynh [14], FR is a unifying framework for high-order methods, capable of recovering existing high-order schemes, and generating new schemes with favorable accuracy and stability properties. Using this framework, Huynh has identified FR schemes for advection–diffusion problems in 1D, and in 2D on quadrilaterals [15] and triangles [16]. In addition, Wang, Gao, Haga, and Yu have identified a closely related class of schemes referred to as Lifting Collocation Penalty (LCP) schemes [17–21] which have recently been extended to handle viscous terms [22]. In 2011, due to the similarity between the FR and LCP methods, the original developers of these methods decided to change their names to Correction Procedure via Reconstruction (CPR) [23,24]. Various CPR schemes have been successfully applied to solve the Navier–Stokes equations in 2D on triangular and quadrilateral elements [17] and in 3D on tetrahedral and prism elements [20,25].

Despite the success of 'FR-type' schemes (i.e. FR and LCP schemes), there remain questions regarding their stability for advection–diffusion problems. Thus far, efforts to prove the stability of the schemes have been incomplete. In particular, in [14,15] Huynh employed Fourier analysis to prove the stability of certain FR schemes. However, this analysis was restricted to uniform grids and a limited range for the order of accuracy. In response, a number of researchers have sought to prove the stability of FR schemes for all orders of accuracy on arbitrary (nonuniform) grids. In particular, in 2010 Jameson used an energy method to prove the stability of a particular SD scheme (an FR-type scheme) for 1D linear advection problems, for all orders of accuracy on nonuniform grids [26]. In numerical experiments, this 'energy stable' SD scheme was shown to exhibit a larger CFL limit than the collocation-based nodal DG scheme [27]. More recently, Vincent, Castonguay, and Jameson identified an entire class of FR schemes which they proved to be stable for linear advection problems in 1D (again for all orders of accuracy on nonuniform grids) [28]. These schemes, referred to as Vincent–Castonguay–Jameson–Huynh (VCJH) schemes [28], are parameterized by a single scalar c, and for particular choices of c, the SD scheme [26] and a collocation-based nodal DG scheme can be obtained for linear problems in 1D.

In this work, a new class of VCJH schemes is developed for solving *advection–diffusion* problems. It will be shown that the schemes are linearly stable on nonuniform grids for all orders of accuracy, thus demonstrating for the first time the stability of a class of FR schemes for advection–diffusion problems.

The format of the paper is as follows. Section two presents a FR approach for solving advection–diffusion problems in 1D. Section three introduces the VCJH correction functions. Section four develops a range of VCJH schemes for linear advection–diffusion problems, and uses an energy method to prove that these schemes are stable for all orders of accuracy. Finally, sections five and six present results of 1D linear and 2D nonlinear numerical experiments, with the aim of assessing how well the new VCJH schemes perform in practice.

2. Flux reconstruction approach for advection–diffusion problems

In this section, a new FR approach for advection–diffusion problems in 1D is presented. For readers unfamiliar with the FR approach for advection problems, the authors recommend a review of the procedure described in [14,28]. For readers unfamiliar with the FR approach for diffusion problems, the authors recommend a review of the procedure described in [15,29]. For the sake of completeness, the following procedure is written for the general class of advection–diffusion problems. In particular, the procedure presented here is applicable for general fluxes $f(u, \frac{\partial u}{\partial x})$ and utilizes distinct flux and solution correction functions.

2.1. Preliminaries

Consider the 1D conservation law

$$\frac{\partial u}{\partial t} + \frac{\partial f}{\partial x} = 0, \tag{1}$$

where x is the spatial coordinate, t is time, $u = u(x,t)$ is the conserved scalar quantity, and the flux $f = f\left(u, \frac{\partial u}{\partial x}\right)$ is a nonlinear function of the solution u and its first spatial derivative. To eliminate terms involving second derivatives of the solution, Eq. (1) can be rewritten as a first-order system, as follows

$$\frac{\partial u}{\partial t} + \frac{\partial}{\partial x}(f(u,q)) = 0, \tag{2}$$

$$q - \frac{\partial u}{\partial x} = 0. \tag{3}$$

This system includes a new variable q, henceforth referred to as the auxiliary variable.

The solution $u = u(x,t)$ to the system defined by Eqs. (2) and (3) evolves in space and time inside an arbitrary 1D spatial domain $\mathbf{\Omega}$. Consider partitioning the domain $\mathbf{\Omega}$ into N non-overlapping, conforming elements each denoted $\mathbf{\Omega}_n = \{x | x_n < x < x_{n+1}\}$ such that

$$\mathbf{\Omega} = \bigcup_{n=1}^{N} \mathbf{\Omega}_n. \tag{4}$$

In Eq. (2), the solution u within $\mathbf{\Omega}_n$ is approximated by a function denoted by $u_n^D = u_n^D(x,t)$, which is a polynomial of degree p inside $\mathbf{\Omega}_n$ and is identically zero outside $\mathbf{\Omega}_n$. The approximate solution is designated with a superscript D to indicate that it is discontinuous in the following sense: the sum of u_n^D and u_{n+1}^D is discontinuous at the boundary between neighbouring elements $\mathbf{\Omega}_n$ and $\mathbf{\Omega}_{n+1}$. The flux f in Eq. (2) can be approximated within each $\mathbf{\Omega}_n$ by a function denoted $f_n = f_n(x,t)$, which is a polynomial of degree $p+1$ inside $\mathbf{\Omega}_n$ and is identically zero outside the element. The sum of f_n and f_{n+1} is required to be C^0-continuous on $\mathbf{\Omega}_n \cup \mathbf{\Omega}_{n+1}$.

Similar approximations can be introduced into Eq. (3). Here, the auxiliary variable q within each $\mathbf{\Omega}_n$ is approximated by a function $q_n^D = q_n^D(x,t)$, which is a polynomial of degree p within $\mathbf{\Omega}_n$ and is identically zero outside the element. In general, the sum of q_n^D and q_{n+1}^D is discontinuous at the boundary between the two elements. Also, in Eq. (3), the solution u within each $\mathbf{\Omega}_n$ is approximated by a function denoted $u_n = u_n(x,t)$, where u_n is a polynomial of degree $p+1$ inside $\mathbf{\Omega}_n$ and is identically zero outside the element. Furthermore, the sum of u_n and u_{n+1} is required to be C^0-continuous on $\mathbf{\Omega}_n \cup \mathbf{\Omega}_{n+1}$ (i.e. $u_n \neq u_n^D$).

Following the introduction of these approximations, the first-order system in each element becomes

$$\frac{\partial u_n^D}{\partial t} + \frac{\partial f_n}{\partial x} = 0, \tag{5}$$

$$q_n^D - \frac{\partial u_n}{\partial x} = 0. \tag{6}$$

For convenience, Eqs. (5) and (6), which were originally formulated on the physical element $\mathbf{\Omega}_n$, can be transformed to the reference element $\mathbf{\Omega}_S = \{r | -1 \leqslant r \leqslant 1\}$ via the mapping

$$x = \Theta_n(r) = \left(\frac{1-r}{2}\right)x_n + \left(\frac{1+r}{2}\right)x_{n+1}. \tag{7}$$

The Jacobian of the mapping is abbreviated J_n and takes the form

$$J_n = \frac{\mathrm{d}\Theta_n}{\mathrm{d}r} = \frac{x_{n+1} - x_n}{2}. \tag{8}$$

Applying this mapping to Eqs. (5) and (6), one obtains

$$\frac{\partial \hat{u}^D}{\partial t} + \frac{\partial \hat{f}}{\partial r} = 0, \tag{9}$$

$$\hat{q}^D - \frac{\partial \hat{u}}{\partial r} = 0, \tag{10}$$

where

$$\hat{u}^D = \hat{u}^D(r,t) = J_n u_n^D(\Theta_n(r),t), \tag{11}$$

$$\hat{q}^D = \hat{q}^D(r,t) = J_n^2 q_n^D(\Theta_n(r),t) \tag{12}$$

are polynomials of degree p, and

$$\hat{f} = \hat{f}(r,t) = f_n(\Theta_n(r),t), \tag{13}$$

$$\hat{u} = \hat{u}(r,t) = J_n u_n(\Theta_n(r),t) \tag{14}$$

are polynomials of degree $p+1$. The evolution of u_n^D within any individual $\mathbf{\Omega}_n$ can be determined by solving the system of transformed equations (Eqs. (9) and (10)) within the standard element $\mathbf{\Omega}_S$.

2.2. Procedure

The FR procedure for solving advection–diffusion problems of the form defined by Eqs. (9) and (10) consists of seven stages. Note that, in practice several of these stages can be combined, however, in what follows they will be presented as separate stages for the sake of clarity.

The first stage defines a form for $\hat{u}^D$ within the standard element $\mathbf{\Omega}_S$. Towards this end, it is assumed that values of the transformed solution $\hat{u}_i^D = \hat{u}_i^D(t)$ are known at a set of $p+1$ solution points ($i = 0$ to p) inside $\mathbf{\Omega}_S$, with each point located at a distinct position r_i. For each solution point i, a Lagrange polynomial $l_i = l_i(r)$ of degree p can be defined as follows

$$l_i = \prod_{j=0, j\neq i}^{p} \left(\frac{r - r_j}{r_i - r_j} \right). \tag{15}$$

The polynomials and the discrete solution values can be used to construct the following expression for $\hat{u}^D$

$$\hat{u}^D = \sum_{i=0}^{p} \hat{u}_i^D \, l_i. \tag{16}$$

The second stage involves calculating a common value of the approximate solution at either end of the standard element $\mathbf{\Omega}_S$ (at $r = \pm 1$). To compute this common solution value, one must first use Eq. (16) to obtain values for the approximate transformed discontinuous solution at both ends of the standard element (where these values are denoted $\hat{u}_L^D = \hat{u}^D(-1,t)$ and $\hat{u}_R^D = \hat{u}^D(1,t)$). Once these values have been obtained, they can be used in conjunction with analogous information from adjoining elements to calculate the common solution values at each interface. Let u_e^I denote the common solution value computed at interface e located between neighboring elements $\mathbf{\Omega}_n$ and $\mathbf{\Omega}_{n+1}$, and let $u_{e,-}^D$ and $u_{e,+}^D$ denote the approximate discontinuous solution on the left and right of interface e, respectively. There are a number of approaches for determining the common solution values at the interfaces, including the Central Flux (CF) [2], local discontinuous Galerkin (LDG) [30], Compact Discontinuous Galerkin (CDG) [31], Interior Penalty (IP) [32], Bassi Rebay 1 (BR1) [6], and Bassi Rebay 2 (BR2) [33] approaches. The LDG approach is of particular interest because it is identical to the CDG approach in 1D, and recovers the BR1 and CF approaches in 1D and in higher dimensions. If one chooses to employ the LDG approach, the common solution value u_e^I is computed as

$$u_e^I = \{\{u_e^D\}\} - \beta [\![u_e^D]\!], \tag{17}$$

where the average $\{\{\cdot\}\}$ and jump $[\![\cdot]\!]$ operators are defined such that

$$\{\{u_e^D\}\} = \frac{u_{e,-}^D + u_{e,+}^D}{2} \tag{18}$$

and

$$[\![u_e^D]\!] = u_{e,-}^D - u_{e,+}^D \tag{19}$$

and where β is a directional parameter which allows u_e^I to assume a value that is biased in either the upwind or downwind direction. Choosing $\beta = \pm 0.5$ ensures that the scheme has a compact stencil in 1D [2,30].

In what follows, the transformed common solution values associated with the left and right ends of the standard element $\mathbf{\Omega}_S$ will be denoted by $\hat{u}_L^I$ and $\hat{u}_R^I$, respectively.

The third stage involves constructing the transformed auxiliary variable $\hat{q}^D$ from the transformed continuous solution $\hat{u} = \hat{u}(r,t)$, where $\hat{u}$ is required to be a degree $p+1$ polynomial in $\mathbf{\Omega}_S$ that takes on the values of the transformed common solutions $\hat{u}_L^I$ and $\hat{u}_R^I$ at the left and right ends of $\mathbf{\Omega}_S$, respectively. The transformed continuous solution $\hat{u}$ is constructed by adding a degree $p+1$ correction $\hat{u}^C = \hat{u}^C(r,t)$ (where the superscript 'C' stands for 'correction') to the transformed discontinuous solution $\hat{u}^D$, such that their sum equals the transformed common solution at the element boundaries ($r = \pm 1$), yet follows (in some sense) the transformed discontinuous solution within the interior of $\mathbf{\Omega}_S$. An expression for $\hat{u}^C$ satisfying these requirements can be formulated by introducing 'correction functions'. Specifically, throughout the element interior $\mathbf{\Omega}_S$, $\hat{u}^C$ takes the form

$$\hat{u}^C = (\hat{u}_L^I - \hat{u}_L^D) g_L + (\hat{u}_R^I - \hat{u}_R^D) g_R, \tag{20}$$

where $g_L = g_L(r)$ and $g_R = g_R(r)$ are correction functions of degree $p+1$ that approximate zero (in some sense) within $\mathbf{\Omega}_S$, as well as satisfying

$$g_L(-1) = 1, \quad g_L(1) = 0, \tag{21}$$

$$g_R(-1) = 0, \quad g_R(1) = 1, \tag{22}$$

and, based on symmetry considerations

$$g_L(r) = g_R(-r). \tag{23}$$

The exact form of g_L and g_R will be discussed in the next section. Using Eq. (20), a degree $p+1$ transformed continuous solution $\hat{u} = \hat{u}(r,t)$ within $\mathbf{\Omega}_S$ can be constructed from the discontinuous solution and the solution correction as follows

$$\hat{u} = \hat{u}^D + \hat{u}^C = \hat{u}^D + (\hat{u}_L^I - \hat{u}_L^D) g_L + (\hat{u}_R^I - \hat{u}_R^D) g_R. \tag{24}$$

Next, an expression for the transformed auxiliary variable $\hat{q}^D$ can be obtained by substituting Eq. (24) into Eq. (10) as follows

$$\hat{q}^D = \frac{\partial \hat{u}}{\partial r} = \frac{\partial \hat{u}^D}{\partial r} + (\hat{u}_L^I - \hat{u}_L^D)\frac{\mathrm{d}g_L}{\mathrm{d}r} + (\hat{u}_R^I - \hat{u}_R^D)\frac{\mathrm{d}g_R}{\mathrm{d}r}. \tag{25}$$

Furthermore, after replacing $\hat{u}^D$ with the definition from Eq. (16), one obtains

$$\hat{q}^D = \sum_{i=0}^{p} \hat{u}_i^D \frac{\mathrm{d}l_i}{\mathrm{d}r} + (\hat{u}_L^I - \hat{u}_L^D)\frac{\mathrm{d}g_L}{\mathrm{d}r} + (\hat{u}_R^I - \hat{u}_R^D)\frac{\mathrm{d}g_R}{\mathrm{d}r}. \tag{26}$$

The fourth stage involves representing the transformed discontinuous flux $\hat{f}^D = \hat{f}^D(r,t)$ using a degree p polynomial within $\mathbf{\Omega}_S$. Towards this end, one first obtains values of the transformed discontinuous flux $\hat{f}_i^D = \hat{f}_i^D(t)$ at each solution point r_i using the transformed discontinuous solution $\hat{u}_i^D$ and the transformed auxiliary variable $\hat{q}_i^D$, i.e. $\hat{f}_i = \hat{f}(\hat{u}_i^D, \hat{q}_i^D)$. Based on these flux values, $\hat{f}^D$ within $\mathbf{\Omega}_S$ is formed as

$$\hat{f}^D = \sum_{i=0}^{p} \hat{f}_i^D \, l_i. \tag{27}$$

The flux $\hat{f}^D$ is termed discontinuous since it is calculated from the transformed solution and the transformed auxiliary variable, both of which are (in general) discontinuous at element boundaries.

The fifth stage involves calculating transformed numerical fluxes at either end of the standard element $\mathbf{\Omega}_S$. This is done by first obtaining values for the approximate transformed discontinuous solution $\hat{u}^D$ and the transformed auxiliary variable $\hat{q}^D$ at both ends of the standard element via Eqs. (16) and (26), respectively. By transforming these values to physical space, one obtains u_L^D, u_R^D, q_L^D, and q_R^D. Once these values have been computed, they can be used in conjunction with analogous information from adjoining elements to calculate transformed numerical interface fluxes. Let f_e^I denote the numerical flux computed at interface e located between neighboring elements $\mathbf{\Omega}_n$ and $\mathbf{\Omega}_{n+1}$. The numerical interface flux f_e^I must be constructed from two separate parts: an advective (inviscid) part $f_{e,adv}^I$ and a diffusive (viscous) part $f_{e,dif}^I$, such that $f_e^I = f_{e,adv}^I + f_{e,dif}^I$. Here $f_{e,adv}^I$ depends on $u_{e,-}^D$ and $u_{e,+}^D$ while $f_{e,dif}^I$ depends on $u_{e,-}^D, u_{e,+}^D, q_{e,-}^D$, and $q_{e,+}^D$. The exact methodology for calculating the numerical fluxes $f_{e,adv}^I$ and $f_{e,dif}^I$ depends on the nature of the equations being solved. For example, when solving the linear advection–diffusion equation, the advective interface flux $f_{e,adv}^I$ is often computed using a Lax–Friedrichs flux, while when solving the Navier–Stokes equations, a Roe [34] or Rusanov [35] type approximate Riemann solver is often employed. The diffusive interface flux $f_{e,dif}^I$ is typically obtained using one of the aforementioned CF, LDG, CDG, IP, BR1, or BR2 approaches. For example, using the LDG approach, the numerical flux $f_{e,dif}^I$ takes the form

$$f_{e,dif}^I = \{\{f_{e,dif}^D\}\} + \tau[\![u_e^D]\!] + \beta[\![f_{e,dif}^D]\!] = \frac{(f_{e,dif,-}^D + f_{e,dif,+}^D)}{2} + \tau(u_{e,-}^D - u_{e,+}^D) + \beta(f_{e,dif,-}^D - f_{e,dif,+}^D), \tag{28}$$

where $f_{e,dif,-}^D = f_{dif}(u_{e,-}^D, q_{e,-}^D), f_{e,dif,+}^D = f_{dif}(u_{e,+}^D, q_{e,+}^D)$, τ is a penalty parameter controlling the jump in the solution, and β is the directional parameter (defined previously). Note that the parameter β in Eq. (28) is preceded by a $+$ sign and in Eq. (17) it is preceded by a $-$ sign. Opposite signs help ensure symmetry of the diffusive process in the following sense: if the common solution u_e^I is upwind biased then the numerical diffusive flux $f_{e,dif}^I$ is downwind biased and conversely if u_e^I is downwind biased then $f_{e,dif}^I$ is upwind biased.

In what follows, the transformed numerical interface fluxes at the left and right ends of the standard element $\mathbf{\Omega}_S$ will be denoted by $\hat{f}_L^I$ and $\hat{f}_R^I$.

The penultimate stage involves constructing a transformed degree $p+1$ total continuous flux $\hat{f} = \hat{f}(r,t)$ in $\mathbf{\Omega}_S$ which takes on the values of the transformed numerical interface fluxes $\hat{f}_L^I$ and $\hat{f}_R^I$ at the left and right ends of $\mathbf{\Omega}_S$, respectively. To construct $\hat{f}$, consider adding a degree $p+1$ transformed correction flux $\hat{f}^C = \hat{f}^C(r,t)$ to the approximate transformed discontinuous flux $\hat{f}^D$, such that their sum equals the transformed numerical interface flux at $r = \pm 1$. In order to define $\hat{f}^C$ such that it satisfies the above requirements, consider introducing degree $p+1$ correction functions $h_L = h_L(r)$ and $h_R = h_R(r)$, which are analogous to g_L and g_R respectively, in the sense that they approximate zero within $\mathbf{\Omega}_S$, as well as satisfying

$$h_L(-1) = 1, \quad h_L(1) = 0, \tag{29}$$

$$h_R(-1) = 0, \quad h_R(1) = 1 \tag{30}$$

and, based on symmetry considerations

$$h_L(r) = h_R(-r). \tag{31}$$

Now, a suitable expression for $\hat{f}^C$ can be written in terms of h_L and h_R as

$$\hat{f}^C = (\hat{f}_L^I - \hat{f}_L^D)h_L + (\hat{f}_R^I - \hat{f}_R^D)h_R, \tag{32}$$

where the transformed discontinuous flux at either end of the element is denoted by $\hat{f}_L^D = \hat{f}^D(-1,t)$ and $\hat{f}_R^D = \hat{f}^D(1,t)$. Using Eq. (32), a degree $p+1$ total continuous transformed flux $\hat{f} = \hat{f}(r,t)$ within $\mathbf{\Omega}_S$ can be constructed from the discontinuous and correction fluxes as follows

$$\hat{f} = \hat{f}^D + \hat{f}^C = \hat{f}^D + (\hat{f}_L^I - \hat{f}_L^D)h_L + (\hat{f}_R^I - \hat{f}_R^D)h_R. \tag{33}$$

The final stage involves using the divergence of $\hat{f}$ to update the transformed solution $\hat{u}_i^D$ at each solution point r_i. The divergence of $\hat{f}$ at the point r_i takes the form

$$\frac{\partial \hat{f}}{\partial r}(r_i) = \sum_{j=0}^{p} \hat{f}_j^D \frac{\mathrm{d}l_j}{\mathrm{d}r}(r_i) + (\hat{f}_L^I - \hat{f}_L^D)\frac{\mathrm{d}h_L}{\mathrm{d}r}(r_i) + (\hat{f}_R^I - \hat{f}_R^D)\frac{\mathrm{d}h_R}{\mathrm{d}r}(r_i). \tag{34}$$

Once the divergence is obtained, it can be used to advance the transformed solution $\hat{u}^D$ in time via a suitable temporal discretization of the following semi-discrete expression

$$\frac{\mathrm{d}\hat{u}_i^D}{\mathrm{d}t} = -\frac{\partial \hat{f}}{\partial r}(r_i). \tag{35}$$

The nature of the FR procedure for advection–diffusion problems in 1D depends solely on five factors, namely:

1. The location of the solution points r_i.
2. The methodology for calculating the transformed common solution values $\hat{u}_L^I$ and $\hat{u}_R^I$ (e.g. CF, LDG, CDG, IP, BR1 or BR2).
3. The methodology for calculating the transformed numerical interface fluxes $\hat{f}_L^I$ and $\hat{f}_R^I$ (e.g. a combination of Lax–Friedrichs, Roe or Rusanov for the advective part and CF, LDG, CDG, IP, BR1 or BR2 for the diffusive part).
4. The form of the solution correction function g_L (and thus by symmetry g_R).
5. The form of the flux correction function h_L (and thus by symmetry h_R).

3. Vincent–Castonguay–Jameson–Huynh correction functions

For linear advection problems in 1D, Vincent et al. [28] recently identified a range of correction functions h_L and h_R for correcting the flux, which lead to energy stable FR schemes for all orders of accuracy. These correction functions will henceforth be referred to as 1D VCJH correction functions. The 1D VCJH left and right corrections functions h_L and h_R are defined as

$$h_L = \frac{(-1)^p}{2}\left[\Psi_p - \left(\frac{\eta_p \Psi_{p-1} + \Psi_{p+1}}{1+\eta_p}\right)\right] \tag{36}$$

and

$$h_R = \frac{1}{2}\left[\Psi_p + \left(\frac{\eta_p \Psi_{p-1} + \Psi_{p+1}}{1+\eta_p}\right)\right], \tag{37}$$

where

$$\eta_p = \frac{c(2p+1)(a_p p!)^2}{2}, a_p = \frac{(2p)!}{2^p (p!)^2}, \tag{38}$$

Ψ_p is a Legendre polynomial of degree p, and c is a free scalar parameter that must lie within the range

$$\frac{-2}{(2p+1)(a_p p!)^2} < c < \infty. \tag{39}$$

The correction functions obtained from Eqs. (36) and (37) lead to VCJH schemes which are an infinite family of FR schemes parameterized by c. For the linear advection equation, it can be noted that several existing methods can be recovered from the class of VCJH schemes. In particular if $c = c_{dg} = 0$, then a collocation-based nodal DG scheme is recovered. Alternatively, if $c = c_{sd}$ (where c_{sd} is defined in [28]), then the SD scheme that Jameson identified in [26] is recovered, and if $c = c_{hu}$ (where c_{hu} is also defined in [28]), then the g_2 FR method that Huynh identified in [14] is recovered. In addition, the analysis presented in [27] identifies a value of c denoted by c_+ which gives an increased explicit time-step limit relative to c_{dg}, c_{sd}, and c_{hu} while maintaining the expected order of accuracy.

Finally, note that stability of the VCJH schemes is ensured for linear advection problems in 1D when periodic boundary conditions are imposed, because for these problems it can be shown that a Sobolev-type norm of the solution is non-increasing, i.e.

$$\frac{d}{dt}\|U^D\|_{p,c}^2 \leqslant 0, \tag{40}$$

where the norm is defined as

$$||U^D||_{p,c} = \left\{\sum_{n=1}^{N}\int_{x_n}^{x_{n+1}}\left[(u_n^D)^2 + \frac{c}{2}(J_n)^{2p}\left(\frac{\partial^p u_n^D}{\partial x^p}\right)^2\right]\mathrm{d}x\right\}^{1/2} \tag{41}$$

and where U^D is the total (domain-wide) solution defined as

$$U^D = \sum_{n=1}^{N} u_n^D. \tag{42}$$

4. Proof of stability of VCJH schemes for the linear advection–diffusion equation

In this section, it is shown that if the correction functions g_L, g_R, h_L, and h_R are chosen to be VCJH correction functions, and the common transformed solution values $\hat{u}_L^I$ and $\hat{u}_R^I$ and numerical flux values $\hat{f}_L^I$ and $\hat{f}_R^I$ are obtained appropriately, the resulting FR schemes are stable for the linear advection–diffusion equation in 1D. The contents of this section are an adaptation of the work done by Castonguay in [36].

4.1. Preliminaries

The linear advection–diffusion equation in 1D takes the form

$$\frac{\partial u}{\partial t} + a\frac{\partial u}{\partial x} - b\frac{\partial^2 u}{\partial x^2} = 0, \tag{43}$$

where a and b are constant scalars (with $b \geqslant 0$). Consider rewriting Eq. (43) as follows

$$\frac{\partial u}{\partial t} + \frac{\partial f}{\partial x} = 0, \quad \text{where } f = au - b\frac{\partial u}{\partial x}.$$

In the reference domain this becomes

$$\frac{\partial \hat{u}}{\partial t} + \frac{\partial \hat{f}}{\partial r} = 0, \quad \text{where } \hat{f} = \hat{a}\hat{u} - \hat{b}\frac{\partial \hat{u}}{\partial r},$$

$\hat{a} = a/J_n$, and $\hat{b} = b/J_n^2$. The approximate transformed discontinuous flux $\hat{f}^D$ evaluated at the solution point r_i is denoted by $\hat{f}_i^D$ and is computed as

$$\hat{f}_i^D = \hat{a}\hat{u}_i^D - \hat{b}\hat{q}_i^D. \tag{44}$$

The evolution in time of the approximate transformed solution $\hat{u}^D$ at the solution point r_i can be determined by combining Eqs. (34), (35), and (44) to obtain

$$\frac{\mathrm{d}\hat{u}_i^D}{\mathrm{d}t} = -\hat{a}\sum_{j=0}^{p}\hat{u}_j^D\frac{\mathrm{d}l_j}{\mathrm{d}r}(r_i) + \hat{b}\sum_{j=0}^{p}\hat{q}_j^D\frac{\mathrm{d}l_j}{\mathrm{d}r}(r_i) - (\hat{f}_L^I - \hat{a}\hat{u}_L^D + \hat{b}\hat{q}_L^D)\frac{\mathrm{d}h_L}{\mathrm{d}r}(r_i) - (\hat{f}_R^I - \hat{a}\hat{u}_R^D + \hat{b}\hat{q}_R^D)\frac{\mathrm{d}h_R}{\mathrm{d}r}(r_i), \tag{45}$$

where $\hat{u}_L^D = \hat{u}^D(-1,t), \hat{u}_R^D = \hat{u}^D(1,t), \hat{q}_L^D = \hat{q}^D(-1,t)$, and $\hat{q}_R^D = \hat{q}^D(1,t)$.

On multiplying Eq. (45) by a Lagrange polynomial l_i, summing over i (from $i = 0$ to p), and simplifying the result, one obtains

$$\frac{\partial \hat{u}^D}{\partial t} = -\hat{a}\frac{\partial \hat{u}^D}{\partial r} + \hat{b}\frac{\partial \hat{q}^D}{\partial r} - (\hat{f}_L^I - \hat{a}\hat{u}_L^D + \hat{b}\hat{q}_L^D)\frac{\mathrm{d}h_L}{\mathrm{d}r} - (\hat{f}_R^I - \hat{a}\hat{u}_R^D + \hat{b}\hat{q}_R^D)\frac{\mathrm{d}h_R}{\mathrm{d}r} = -\frac{\partial \hat{f}^D}{\partial r} - (\hat{f}_L^I - \hat{f}_L^D)\frac{\mathrm{d}h_L}{\mathrm{d}r} - (\hat{f}_R^I - \hat{f}_R^D)\frac{\mathrm{d}h_R}{\mathrm{d}r}. \tag{46}$$

Eq. (46) governs the temporal evolution of $\hat{u}^D$ within $\mathbf{\Omega}_S$.

4.2. The stability of VCJH schemes

The stability of VCJH schemes for the linear advection–diffusion equation in 1D can be demonstrated by looking at the evolution in time of the norm given by Eq. (41). For the linear advection–diffusion equation, the time rate of change of this norm depends on contributions from the transformed solution $\hat{u}^D$ (i.e. Eq. (46)) and the transformed auxiliary variable $\hat{q}^D$ (i.e. Eq. (25)). The following lemmas identify key results associated with both equations and thereafter these results are used to prove the stability of the VCJH schemes.

Lemma 4.1. *For all FR schemes, Eq. (46) holds, and therefore the following results also hold*

$$\frac{1}{2}\frac{\mathrm{d}}{\mathrm{d}t}\int_{-1}^{1}(\hat{u}^D)^2\mathrm{d}r = -\int_{-1}^{1}\hat{u}^D\frac{\partial \hat{f}^D}{\partial r}\mathrm{d}r - (\hat{f}_L^I - \hat{f}_L^D)\int_{-1}^{1}\hat{u}^D\frac{\mathrm{d}h_L}{\mathrm{d}r}\mathrm{d}r - (\hat{f}_R^I - \hat{f}_R^D)\int_{-1}^{1}\hat{u}^D\frac{\mathrm{d}h_R}{\mathrm{d}r}\mathrm{d}r \tag{47}$$

and

$$\frac{1}{2}\frac{\mathrm{d}}{\mathrm{d}t}\int_{-1}^{1}\left(\frac{\partial^p \hat{u}^D}{\partial r^p}\right)^2\mathrm{d}r = -2(\hat{f}_L^I - \hat{f}_L^D)\left(\frac{\partial^p \hat{u}^D}{\partial r^p}\right)\left(\frac{\mathrm{d}^{p+1}h_L}{\mathrm{d}r^{p+1}}\right) - 2(\hat{f}_R^I - \hat{f}_R^D)\left(\frac{\partial^p \hat{u}^D}{\partial r^p}\right)\left(\frac{\mathrm{d}^{p+1}h_R}{\mathrm{d}r^{p+1}}\right). \tag{48}$$

Proof. Consider multiplying Eq. (46) by $\hat{u}^D$ and integrating over the reference domain $\mathbf{\Omega}_S$, to obtain

$$\int_{-1}^{1} \hat{u}^D \frac{\partial \hat{u}^D}{\partial t} \mathrm{d}r = -\int_{-1}^{1} \hat{u}^D \frac{\partial \hat{f}^D}{\partial r} \mathrm{d}r - (\hat{f}_L^I - \hat{f}_L^D) \int_{-1}^{1} \hat{u}^D \frac{\mathrm{d}h_L}{\mathrm{d}r} \mathrm{d}r - (\hat{f}_R^I - \hat{f}_R^D) \int_{-1}^{1} \hat{u}^D \frac{\mathrm{d}h_R}{\mathrm{d}r} \mathrm{d}r, \tag{49}$$

from which Eq. (47) follows immediately.

On differentiating Eq. (46) p times (in space) one obtains

$$\frac{\partial}{\partial t}\left(\frac{\partial^p \hat{u}^D}{\partial r^p}\right) = -\frac{\partial^{p+1} \hat{f}^D}{\partial r^{p+1}} - (\hat{f}_L^I - \hat{f}_L^D)\frac{\mathrm{d}^{p+1} h_L}{\mathrm{d}r^{p+1}} - (\hat{f}_R^I - \hat{f}_R^D)\frac{\mathrm{d}^{p+1} h_R}{\mathrm{d}r^{p+1}}, \tag{50}$$

where $\hat{f}^D$ is a polynomials of degree p and $\frac{\partial^{p+1}\hat{f}^D}{\partial r^{p+1}} = 0$. On multiplying Eq. (50) by the p^{th} derivative of the approximate transformed solution $\hat{u}^D$ and integrating over $\mathbf{\Omega}_S$, one obtains

$$\int_{-1}^{1} \left(\frac{\partial^p \hat{u}^D}{\partial r^p}\right) \frac{\partial}{\partial t}\left(\frac{\partial^p \hat{u}^D}{\partial r^p}\right) \mathrm{d}r = -(\hat{f}_L^I - \hat{f}_L^D) \int_{-1}^{1} \left(\frac{\partial^p \hat{u}^D}{\partial r^p}\right)\left(\frac{\mathrm{d}^{p+1} h_L}{\mathrm{d}r^{p+1}}\right) \mathrm{d}r - (\hat{f}_R^I - \hat{f}_R^D) \int_{-1}^{1} \left(\frac{\partial^p \hat{u}^D}{\partial r^p}\right)\left(\frac{\mathrm{d}^{p+1} h_R}{\mathrm{d}r^{p+1}}\right) \mathrm{d}r, \tag{51}$$

from which Eq. (48) follows immediately. This completes the proof of Lemma 4.1. □

Lemma 4.2. *For all FR schemes, Eq. (25) holds, and therefore the following results also hold*

$$\int_{-1}^{1} (\hat{q}^D)^2 \mathrm{d}r = \int_{-1}^{1} \hat{q}^D \frac{\partial \hat{u}^D}{\partial r} \mathrm{d}r + (\hat{u}_L^I - \hat{u}_L^D) \int_{-1}^{1} \hat{q}^D \frac{\mathrm{d}g_L}{\mathrm{d}r} \mathrm{d}r + (\hat{u}_R^I - \hat{u}_R^D) \int_{-1}^{1} \hat{q}^D \frac{\mathrm{d}g_R}{\mathrm{d}r} \mathrm{d}r \tag{52}$$

and

$$\int_{-1}^{1} \left(\frac{\partial^p \hat{q}^D}{\partial r^p}\right)^2 \mathrm{d}r = 2(\hat{u}_L^I - \hat{u}_L^D)\left(\frac{\partial^p \hat{q}^D}{\partial r^p}\right)\left(\frac{\mathrm{d}^{p+1} g_L}{\mathrm{d}r^{p+1}}\right) + 2(\hat{u}_R^I - \hat{u}_R^D)\left(\frac{\partial^p \hat{q}^D}{\partial r^p}\right)\left(\frac{\mathrm{d}^{p+1} g_R}{\mathrm{d}r^{p+1}}\right). \tag{53}$$

Proof. Eq. (52) follows from multiplying Eq. (25) by $\hat{q}^D$ and integrating over the reference domain $\mathbf{\Omega}_S$. Eq. (53) follows from differentiating Eq. (25) p times in space, observing that $\frac{\partial^{p+1}\hat{q}^D}{\partial r^{p+1}} = 0$, multiplying by the p^{th} derivative of $\hat{q}^D$, and integrating over $\mathbf{\Omega}_S$. This completes the proof of Lemma 4.2. □

Lemma 4.3. *If h_L, h_R, g_L, and g_R are the VCJH correction functions, the following identity holds*

$$\begin{aligned}
&\frac{1}{2}\frac{\mathrm{d}}{\mathrm{d}t}\int_{-1}^{1}\left[(\hat{u}^D)^2 + \frac{c}{2}\left(\frac{\partial^p \hat{u}^D}{\partial r^p}\right)^2\right]\mathrm{d}r + \hat{b}\int_{-1}^{1}\left[(\hat{q}^D)^2 + \frac{\kappa}{2}\left(\frac{\partial^p \hat{q}^D}{\partial r^p}\right)^2\right]\mathrm{d}r \\
&\quad = -\int_{-1}^{1} \hat{u}^D \frac{\partial \hat{f}^D}{\partial r}\mathrm{d}r + \hat{b}\int_{-1}^{1} \hat{q}^D \frac{\partial \hat{u}^D}{\partial r}\mathrm{d}r + (\hat{f}_L^I - \hat{f}_L^D)\hat{u}_L^D - (\hat{f}_R^I - \hat{f}_R^D)\hat{u}_R^D - \hat{b}(\hat{u}_L^I - \hat{u}_L^D)\hat{q}_L^D + \hat{b}(\hat{u}_R^I - \hat{u}_R^D)\hat{q}_R^D,
\end{aligned} \tag{54}$$

where c and κ are constants which parameterize the VCJH correction functions h_L (and thus h_R) and g_L (and thus g_R), respectively, and where in general it is assumed that $c \neq \kappa$.

Proof. Upon multiplying Eq. (52) by $\hat{b}$ and adding it to Eq. (47) one obtains

$$\begin{aligned}
\frac{1}{2}\frac{\mathrm{d}}{\mathrm{d}t}\int_{-1}^{1}(\hat{u}^D)^2\mathrm{d}r + \hat{b}\int_{-1}^{1}(\hat{q}^D)^2\mathrm{d}r &= -\int_{-1}^{1}\hat{u}^D\frac{\partial \hat{f}^D}{\partial r}\mathrm{d}r + \hat{b}\int_{-1}^{1}\hat{q}^D\frac{\partial \hat{u}^D}{\partial r}\mathrm{d}r - (\hat{f}_L^I - \hat{f}_L^D)\int_{-1}^{1}\hat{u}^D\frac{\mathrm{d}h_L}{\mathrm{d}r}\mathrm{d}r - (\hat{f}_R^I - \hat{f}_R^D)\int_{-1}^{1}\hat{u}^D\frac{\mathrm{d}h_R}{\mathrm{d}r}\mathrm{d}r \\
&\quad + \hat{b}(\hat{u}_L^I - \hat{u}_L^D)\int_{-1}^{1}\hat{q}^D\frac{\mathrm{d}g_L}{\mathrm{d}r}\mathrm{d}r + \hat{b}(\hat{u}_R^I - \hat{u}_R^D)\int_{-1}^{1}\hat{q}^D\frac{\mathrm{d}g_R}{\mathrm{d}r}\mathrm{d}r.
\end{aligned} \tag{55}$$

Using integration by parts, the right hand side (RHS) can be rewritten as

$$\begin{aligned}
\frac{1}{2}\frac{\mathrm{d}}{\mathrm{d}t}\int_{-1}^{1}(\hat{u}^D)^2\mathrm{d}r + \hat{b}\int_{-1}^{1}(\hat{q}^D)^2\mathrm{d}r &= -\int_{-1}^{1}\hat{u}^D\frac{\partial \hat{f}^D}{\partial r}\mathrm{d}r + \hat{b}\int_{-1}^{1}\hat{q}^D\frac{\partial \hat{u}^D}{\partial r}\mathrm{d}r - (\hat{f}_L^I - \hat{f}_L^D)\left[-\int_{-1}^{1}h_L\frac{\partial \hat{u}^D}{\partial r}\mathrm{d}r - \hat{u}_L^D\right] \\
&\quad - (\hat{f}_R^I - \hat{f}_R^D)\left[-\int_{-1}^{1}h_R\frac{\partial \hat{u}^D}{\partial r}\mathrm{d}r + \hat{u}_R^D\right] + \hat{b}(\hat{u}_L^I - \hat{u}_L^D)\left[-\int_{-1}^{1}g_L\frac{\partial \hat{q}^D}{\partial r}\mathrm{d}r - \hat{q}_L^D\right] \\
&\quad + \hat{b}(\hat{u}_R^I - \hat{u}_R^D)\left[-\int_{-1}^{1}g_R\frac{\partial \hat{q}^D}{\partial r}\mathrm{d}r + \hat{q}_R^D\right].
\end{aligned} \tag{56}$$

Furthermore, on multiplying Eq. (48) by c and Eq. (53) by $\hat{b}\kappa$, and adding the result to Eq. (56), one obtains

$$\frac{1}{2}\frac{\mathrm{d}}{\mathrm{d}t}\int_{-1}^{1}(\hat{u}^D)^2\mathrm{d}r+\frac{c}{4}\frac{\mathrm{d}}{\mathrm{d}t}\int_{-1}^{1}\left(\frac{\partial^p\hat{u}^D}{\partial r^p}\right)^2\mathrm{d}r+\hat{b}\int_{-1}^{1}(\hat{q}^D)^2\mathrm{d}r+\frac{\hat{b}\kappa}{2}\int_{-1}^{1}\left(\frac{\partial^p\hat{q}^D}{\partial r^p}\right)^2\mathrm{d}r$$
$$=-\int_{-1}^{1}\hat{u}^D\frac{\partial\hat{f}^D}{\partial r}\mathrm{d}r+\hat{b}\int_{-1}^{1}\hat{q}^D\frac{\partial\hat{u}^D}{\partial r}\mathrm{d}r-(\hat{f}_L^I-\hat{f}_L^D)\left[-\hat{u}_L^D-\int_{-1}^{1}h_L\frac{\partial\hat{u}^D}{\partial r}\mathrm{d}r+c\left(\frac{\partial^p\hat{u}^D}{\partial r^p}\right)\left(\frac{\mathrm{d}^{p+1}h_L}{\mathrm{d}r^{p+1}}\right)\right]-(\hat{f}_R^I$$
$$-\hat{f}_R^D)\left[\hat{u}_R^D-\int_{-1}^{1}h_R\frac{\partial\hat{u}^D}{\partial r}\mathrm{d}r+c\left(\frac{\partial^p\hat{u}^D}{\partial r^p}\right)\left(\frac{\mathrm{d}^{p+1}h_R}{\mathrm{d}r^{p+1}}\right)\right]+\hat{b}(\hat{u}_L^I-\hat{u}_L^D)\left[-\hat{q}_L^D-\int_{-1}^{1}g_L\frac{\partial\hat{q}^D}{\partial r}\mathrm{d}r+\kappa\left(\frac{\partial^p\hat{q}^D}{\partial r^p}\right)\left(\frac{\mathrm{d}^{p+1}g_L}{\mathrm{d}r^{p+1}}\right)\right]$$
$$+\hat{b}(\hat{u}_R^I-\hat{u}_R^D)\left[\hat{q}_R^D-\int_{-1}^{1}g_R\frac{\partial\hat{q}^D}{\partial r}\mathrm{d}r+\kappa\left(\frac{\partial^p\hat{q}^D}{\partial r^p}\right)\left(\frac{\mathrm{d}^{p+1}g_R}{\mathrm{d}r^{p+1}}\right)\right]. \tag{57}$$

Since h_L, h_R, g_L, and g_R are the VCJH correction functions, they satisfy the following identities (as shown in [28])

$$\int_{-1}^{1}h_L\frac{\partial l_i}{\partial r}\mathrm{d}r-c\left(\frac{\mathrm{d}^{p+1}h_L}{\mathrm{d}r^{p+1}}\right)\left(\frac{\partial^p l_i}{\partial r^p}\right)=0,\quad \int_{-1}^{1}h_R\frac{\partial l_i}{\partial r}\mathrm{d}r-c\left(\frac{\mathrm{d}^{p+1}h_R}{\mathrm{d}r^{p+1}}\right)\left(\frac{\partial^p l_i}{\partial r^p}\right)=0, \tag{58}$$

$$\int_{-1}^{1}g_L\frac{\partial l_i}{\partial r}\mathrm{d}r-\kappa\left(\frac{\mathrm{d}^{p+1}g_L}{\mathrm{d}r^{p+1}}\right)\left(\frac{\partial^p l_i}{\partial r^p}\right)=0,\quad \int_{-1}^{1}g_R\frac{\partial l_i}{\partial r}\mathrm{d}r-\kappa\left(\frac{\mathrm{d}^{p+1}g_R}{\mathrm{d}r^{p+1}}\right)\left(\frac{\partial^p l_i}{\partial r^p}\right)=0. \tag{59}$$

Eqs. (58) and (59) can be rewritten with $\hat{u}^D$ or $\hat{q}^D$ in place of l_i as follows

$$-\int_{-1}^{1}h_L\frac{\partial\hat{u}^D}{\partial r}\mathrm{d}r+c\int_{-1}^{1}\left(\frac{\mathrm{d}^{p+1}h_L}{\mathrm{d}r^{p+1}}\right)\left(\frac{\partial^p\hat{u}^D}{\partial r^p}\right)\mathrm{d}r=0, \tag{60}$$

$$-\int_{-1}^{1}h_R\frac{\partial\hat{u}^D}{\partial r}\mathrm{d}r+c\int_{-1}^{1}\left(\frac{\mathrm{d}^{p+1}h_R}{\mathrm{d}r^{p+1}}\right)\left(\frac{\partial^p\hat{u}^D}{\partial r^p}\right)\mathrm{d}r=0, \tag{61}$$

$$-\int_{-1}^{1}g_L\frac{\partial\hat{q}^D}{\partial r}\mathrm{d}r+\kappa\int_{-1}^{1}\left(\frac{\mathrm{d}^{p+1}g_L}{\mathrm{d}r^{p+1}}\right)\left(\frac{\partial^p\hat{q}^D}{\partial r^p}\right)\mathrm{d}r=0, \tag{62}$$

$$-\int_{-1}^{1}g_R\frac{\partial\hat{q}^D}{\partial r}\mathrm{d}r+\kappa\int_{-1}^{1}\left(\frac{\mathrm{d}^{p+1}g_R}{\mathrm{d}r^{p+1}}\right)\left(\frac{\partial^p\hat{q}^D}{\partial r^p}\right)\mathrm{d}r=0, \tag{63}$$

where the fact that $\hat{u}^D$ and $\hat{q}^D$ are polynomials of degree p and can be written as linear combinations of the Lagrange polynomials l_i has been used. Eq. (54) follows immediately from substituting Eqs. (60)–(63) into Eq. (57). This completes the proof of Lemma 4.3. □

Theorem 4.1. *If VCJH schemes (for which Lemmas 4.1, 4.2 and 4.3 hold) are employed in conjunction with a Lax–Friedrichs formulation for the advective numerical flux f_{adv}^I, and the LDG formulation for the common solution u^I and diffusive numerical flux f_{dif}^I, then the following result holds*

$$\frac{\mathrm{d}}{\mathrm{d}t}\|U^D\|_{p,c}^2\leqslant 0. \tag{64}$$

Proof. Eq. (54) (the result of Lemma 4.3) can be reformulated based on the identities

$$\int_{-1}^{1}\hat{u}^D\frac{\partial\hat{q}^D}{\partial r}\mathrm{d}r+\int_{-1}^{1}\hat{q}^D\frac{\partial\hat{u}^D}{\partial r}\mathrm{d}r=\int_{-1}^{1}\frac{\partial(\hat{u}^D\hat{q}^D)}{\partial r}\mathrm{d}r=\hat{u}_R^D\hat{q}_R^D-\hat{u}_L^D\hat{q}_L^D, \tag{65}$$

$$\int_{-1}^{1}\hat{u}^D\frac{\partial\hat{u}^D}{\partial r}\mathrm{d}r=\frac{1}{2}\left[(\hat{u}_R^D)^2-(\hat{u}_L^D)^2\right] \tag{66}$$

and the definition of the transformed discontinuous flux $\hat{f}^D=\hat{a}\hat{u}^D-\hat{b}\hat{q}^D$, yielding

$$\frac{1}{2}\frac{\mathrm{d}}{\mathrm{d}t}\int_{-1}^{1}\left[(\hat{u}^D)^2+\frac{c}{2}\left(\frac{\partial^p\hat{u}^D}{\partial r^p}\right)^2\right]\mathrm{d}r+\hat{b}\int_{-1}^{1}\left[(\hat{q}^D)^2+\frac{\kappa}{2}\left(\frac{\partial^p\hat{q}^D}{\partial r^p}\right)^2\right]\mathrm{d}r$$
$$=-\frac{\hat{a}}{2}\left((\hat{u}_R^D)^2-(\hat{u}_L^D)^2\right)+\hat{b}(\hat{u}_R^D\hat{q}_R^D-\hat{u}_L^D\hat{q}_L^D)+(\hat{f}_L^I-\hat{a}\hat{u}_L^D+\hat{b}\hat{q}_L^D)\hat{u}_L^D-(\hat{f}_R^I-\hat{a}\hat{u}_R^D+\hat{b}\hat{q}_R^D)\hat{u}_R^D-\hat{b}(\hat{u}_L^I-\hat{u}_L^D)\hat{q}_L^D+\hat{b}(\hat{u}_R^I-\hat{u}_R^D)\hat{q}_R^D. \tag{67}$$

Consider transforming Eq. (67) into physical space, in order to obtain

$$\frac{1}{2}\frac{\mathrm{d}}{\mathrm{d}t}\int_{\Omega_n}\left[(u_n^D)^2+\frac{c}{2}(J_n)^{2p}\left(\frac{\partial^p u_n^D}{\partial x^p}\right)^2\right]\mathrm{d}x+b\int_{\Omega_n}\left[(q_n^D)^2+\frac{\kappa}{2}(J_n)^{2p}\left(\frac{\partial^p q_n^D}{\partial x^p}\right)^2\right]\mathrm{d}x$$
$$=\left[-\frac{a}{2}\left((u_R^D)^2-(u_L^D)^2\right)+b(u_R^D q_R^D-u_L^D q_L^D)+(f_L^I-au_L^D+bq_L^D)u_L^D-(f_R^I-au_R^D+bq_R^D)u_R^D-b(u_L^I-u_L^D)q_L^D+b(u_R^I-u_R^D)q_R^D\right]_n. \tag{68}$$

Now consider summing over all the elements, assuming a periodic domain, in order to obtain

$$\frac{1}{2}\frac{\mathrm{d}}{\mathrm{d}t}\|U^D\|_{p,c}^2=-b\|Q^D\|_{p,\kappa}^2+\sum_{e=1}^{N_e}\Theta_e, \tag{69}$$

where Θ_e is the contribution from interface e located between elements $\boldsymbol{\Omega}_n$ and $\boldsymbol{\Omega}_{n+1}$, N_e is the total number of edges, and

$$\|U^D\|_{p,c}=\left\{\sum_{n=1}^{N}\int_{x_n}^{x_{n+1}}\left[(u_n^D)^2+\frac{c}{2}(J_n)^{2p}\left(\frac{\partial^p u_n^D}{\partial x^p}\right)^2\right]\mathrm{d}x\right\}^{1/2} \tag{70}$$

and

$$\|Q^D\|_{p,\kappa}=\left\{\sum_{n=1}^{N}\int_{x_n}^{x_{n+1}}\left[(q_n^D)^2+\frac{\kappa}{2}(J_n)^{2p}\left(\frac{\partial^p q_n^D}{\partial x^p}\right)^2\right]\mathrm{d}x\right\}^{1/2}, \tag{71}$$

are both norms if the values of c and κ lie in the range given by Eq. (39), as shown in [28]. From Eq. (68), Θ_e takes the form

$$\Theta_e=\frac{a}{2}(u_{e,-}^D)^2-\frac{a}{2}(u_{e,+}^D)^2+bu_{e,+}^D q_{e,+}^D-bu_{e,-}^D q_{e,-}^D+f_e^I\left(u_{e,+}^D-u_{e,-}^D\right)-bu_e^I\left(q_{e,+}^D-q_{e,-}^D\right), \tag{72}$$

where the subscripts $+$ and $-$ refer to quantities on the right and left of interface e respectively, f_e^I is the common numerical flux, and u_e^I is the common solution, both of which are also associated with interface e. In general, the common numerical flux f_e^I is divided into two separate components $f_e^I=f_{e,adv}^I+f_{e,dif}^I$, where $f_{e,adv}^I=(au)_e^I$ and $f_{e,dif}^I=-(bq)_e^I$. In what follows, it will be shown that if $f_{e,adv}^I$ is computed using a Lax–Friedrichs flux and if $f_{e,dif}^I$ is computed using the LDG approach, then $\Theta_e\leqslant 0$.

Using a Lax–Friedrichs flux, the common advective numerical flux is computed as

$$f_{e,adv}^I=\{\{au_e^D\}\}+\frac{\lambda}{2}|a|[\![u_e^D]\!], \tag{73}$$

where λ is an upwinding parameter such that $0\leqslant\lambda\leqslant 1$. Note that $\lambda=0$ recovers a central scheme while $\lambda=1$ recovers a fully upwind scheme. With the LDG approach, the common approximate solution u_e^I and the common diffusive numerical flux $f_{e,dif}^I$ are computed as

$$u_e^I=\{\{u_e^D\}\}-\beta[\![u_e^D]\!] \tag{74}$$

and

$$f_{e,dif}^I=\{\{-bq_e^D\}\}+\tau[\![u_e^D]\!]+\beta[\![-bq_e^D]\!], \tag{75}$$

respectively, where β is a directional parameter and τ is a penalty parameter. Note that for the choice $\beta=0$ and $\tau=0$, the BR1 approach of Bassi and Rebay is recovered while for $\beta\neq 0$ and $\tau=0$, the CF approach is recovered.

For these choices of the common numerical fluxes and common approximate solution, the contribution from each interface becomes

$$\begin{aligned}\Theta_e=&\frac{a}{2}(u_{e,-}^D)^2-\frac{a}{2}(u_{e,+}^D)^2+\left[\{\{au_e^D\}\}+\frac{\lambda}{2}|a|[\![u_e^D]\!]\right]u_{e,+}^D-\left[\{\{au_e^D\}\}+\frac{\lambda}{2}|a|[\![u_e^D]\!]\right]u_{e,-}^D\\&+\left[\{\{-bq_e^D\}\}+\tau[\![u_e^D]\!]+\beta[\![-bq_e^D]\!]\right]u_{e,+}^D-\left[\{\{-bq_e^D\}\}+\tau[\![u_e^D]\!]+\beta[\![-bq_e^D]\!]\right]u_{e,-}^D-b\left[\{\{u_e^D\}\}-\beta[\![u_e^D]\!]\right]q_{e,+}^D\\&+bu_{e,+}^D q_{e,+}^D+b\left[\{\{u_e^D\}\}-\beta[\![u_e^D]\!]\right]q_{e,-}^D-bu_{e,-}^D q_{e,-}^D\\=&-\frac{\lambda}{2}|a|\left(u_{e,+}^D-u_{e,-}^D\right)^2-\tau(u_{e,+}^D-u_{e,-}^D)^2\end{aligned} \tag{76}$$

and Eq. (69) becomes

$$\frac{1}{2}\frac{\mathrm{d}}{\mathrm{d}t}\|U^D\|_{p,c}^2=-b\|Q^D\|_{p,\kappa}^2-\sum_{e=1}^{N_e}\left[\frac{\lambda}{2}|a|\left(u_{e,+}^D-u_{e,-}^D\right)^2+\tau(u_{e,+}^D-u_{e,-}^D)^2\right]. \tag{77}$$

Since $b\geqslant 0,\lambda\geqslant 0$, and $\tau\geqslant 0$, Eq. (64) immediately follows from Eq. (77). This completes the proof of Theorem 4.1. □

Remark. Theorem 4.1 proves that the time rate of change of $\|U^D\|^2_{p,c}$ is non-positive, hence the approximate solution U^D is bounded in the norm defined by Eq. (41), and hence in all norms via the equivalence of norms in a finite dimensional space. This result guarantees stability of the VCJH schemes for the linear advection–diffusion equation in 1D. Stability of the schemes has been established with no assumptions regarding the uniformity of the mesh, the order of the solution polynomials p, or the position of the solution points.

In summary, Theorem 4.1 was obtained assuming that:

1. The correction functions h_L, h_R, g_L, and g_R are chosen to be the VCJH correction functions defined by Eqs. (36)–(39). This guarantees that the identities in Eqs. (60)–(63) hold, and that the constants c and κ are such that $\|U^D\|_{p,c}$ and $\|Q^D\|_{p,\kappa}$ are norms.
2. The advective numerical flux is defined in accordance with a Lax–Friedrichs approach (Eq. (73)).
3. The common approximate solution and the diffusive numerical flux are defined in accordance with the LDG approach (Eqs. (74) and (75), respectively).

Finally, note that although the stability proof has been constructed for the specific case in which a Lax–Friedrichs flux is used for the advective numerical flux and the LDG approach is used for the common solution and diffusive numerical flux, the proof still has broad applicability. The Lax–Friedrichs and LDG approaches are quite general because, as discussed previously, the former recovers both the central and upwind approaches, and the latter recovers the CDG, BR1, and CF approaches in 1D. It should be noted however that although stability was shown for arbitrary values of λ in the range $0 \leqslant \lambda \leqslant 1$, using a value of $\lambda = 0$ is not advisable since for pure advection problems ($b = 0$), VCJH schemes are at the limit of stability.

5. One-dimensional linear numerical experiments

In this section, orders of accuracy and explicit time-step limits of VCJH schemes are examined via numerical experiments on the 1D linear advection–diffusion equation.

Consider the 1D advection–diffusion of a scalar $u = u(x,t)$ governed by Eq. (43) with $x \in [0, 2\pi]$, an initial condition $u(x,0) = \sin(x)$, and periodic boundary conditions. This problem has an analytical solution, $u^e = \exp(-bt)\sin(x - at)$.

Approximate solutions were obtained using the 1D VCJH schemes for advection–diffusion problems in conjunction with an explicit, low-storage, 5 stage, 4th order Runge–Kutta scheme for time advancement (denoted RK54) [37], the Lax–Friedrichs approach (with $\lambda = 1$) for the computation of the advective numerical fluxes, and the LDG approach for the computation of the common solution values and diffusive numerical fluxes. Numerical experiments were performed using different values of c and κ, which determine the correction functions, and different values of β and τ, which determine the LDG scheme. Values for these parameters were selected as follows.

- Choosing c and κ: The four values of c discussed in Section 3 are known to possess favorable accuracy and stability properties for linear advection problems. These four values of c ($c = c_{dg}, c = c_{sd}, c = c_{hu}$, and $c = c_+$) were therefore chosen for the experiments. For the explicit time-step limit study, four equivalent values of κ ($\kappa = \kappa_{dg} = c_{dg}, \kappa = \kappa_{sd} = c_{sd}, \kappa = \kappa_{hu} = c_{hu}$, and $\kappa = \kappa_+ = c_+$) were used. Table (1) shows numerical values of c and κ, for $p = 2$ to 4. Note that the values of c_+ and κ_+ in Table (1) are valid only for the RK54 time-stepping scheme, and the reader is referred to [27] for values of c_+ and κ_+ for other time-stepping schemes.
- Choosing β: For time-dependent diffusion problems, Cockburn and Shu [30] observed that a value of $\beta \neq 0$ is required for preserving the order of accuracy of a DG scheme paired with an LDG-type flux. Thus, for all numerical experiments, a value of $\beta = 0.5$ was chosen. This value of β ensures the compactness of the scheme in 1D (as mentioned previously).
- Choosing τ: For elliptic problems, Castillo et al. [38] demonstrated that choosing $\tau \sim 1$ preserves the accuracy and stability of DG schemes. However, for time-dependent problems, Hesthaven and Warburton [2] demonstrated that accuracy and stability can be obtained with $\tau = 0$. Taking into account the results from references [38,2], experiments were performed with both zero and nonzero values of τ ($\tau = 0$, 0.1, and 1).

5.1. Order of accuracy results

The spatial order of accuracy for each scheme was evaluated based on the L2 norm of the solution error ($E^{(L2)}$) and the L2 semi-norm of the solution gradient error ($E^{(L2s)}$), which were each computed as follows

Table 1
Reference values of c and κ used in the 1D linear numerical experiments (taken from [27]).

	p = 2	p = 3	p = 4
$c_{dg} = \kappa_{dg}$	0	0	0
$c_{sd} = \kappa_{sd}$	2.96e−2	9.52e−4	1.61e−5
$c_{hu} = \kappa_{hu}$	6.67e−2	1.69e−3	2.52e−5
$c_+ = \kappa_+$	2.06e−1	3.80e−3	4.67e−5

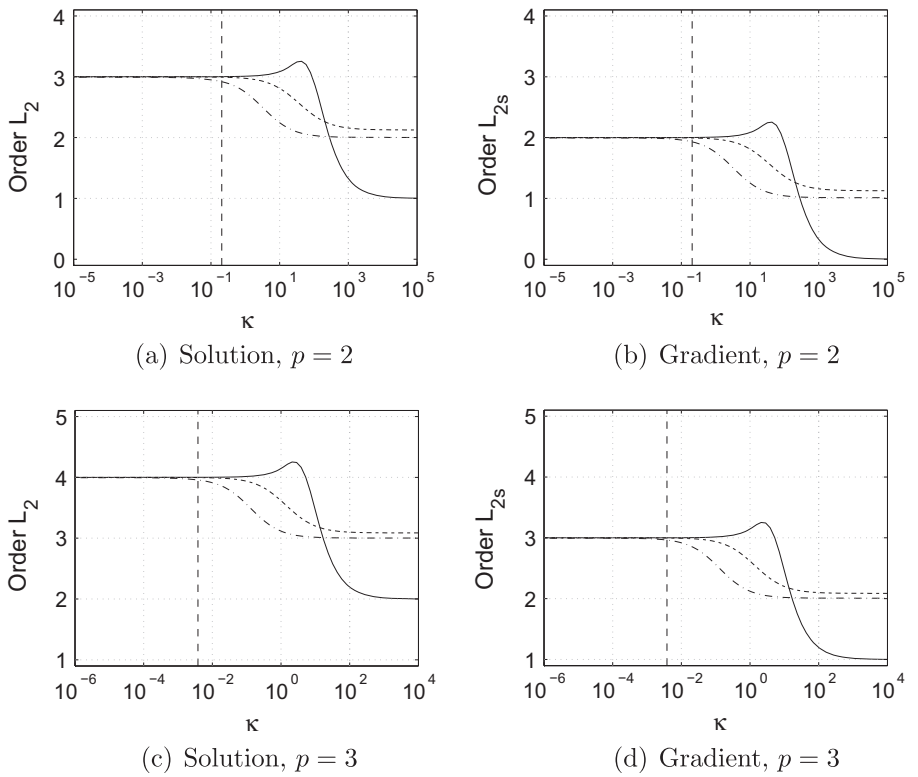

Fig. 1. Plots of the order of accuracy with which $E^{(L2)}$ and $E^{(L2s)}$ converge for VCJH schemes with $c = c_{sd}, \beta = 0.5$, and $\kappa \in [10^{-6}, 10^{5}]$, on the model linear advection–diffusion problem with $a = 0, b = 1$, and $p = 2$ and $p = 3$. Results for $\tau = 0$, 0.1, and 1 are denoted by solid, dashed, and dot-dashed curves, respectively. A vertical dashed line marks the location of $\kappa = \kappa_+ = c_+$.

$$E^{(L2)} = \sqrt{\sum_{n=1}^{N} \int_{\Omega_n} (u^e - u_n^D)^2 \, d\Omega_n}, \quad E^{(L2s)} = \sqrt{\sum_{n=1}^{N} \int_{\Omega_n} \left(\frac{\partial u^e}{\partial x} - \frac{\partial u_n^D}{\partial x} \right)^2 d\Omega_n}, \tag{78}$$

where integrals over each element Ω_n were evaluated using a quadrature rule of sufficient strength. Note that $E^{(L2)}$ is expected to converge at a rate of h^{p+1}, and $E^{(L2s)}$ is expected to converge at a rate of h^p [39], where h is the mesh spacing.

In the following, the order of accuracy was evaluated on uniform grids with $N = 32$, 48, and 64 elements for cases in which $p = 2$ and $p = 3$. In each case, the time-step was chosen sufficiently small to ensure that temporal errors were negligible relative to spatial errors. For each set of grids, a single, representative value for the order of accuracy was computed using the slope of a linear least-squares fit of error vs. mesh spacing on a log scale. For each curve-fit, the correlation coefficient exceeded 0.977.

Figs. (1) and (2) show the order of accuracy with which the solution and its gradient converge for schemes with κ varying in the range $\left[10^{-6}, 10^{5}\right]$ and fixed parameters: $c = c_{sd}, \beta = 0.5$, and $\tau = 0$, 0.1, and 1. Experiments were performed for each of the four values of c (c_{dg}, c_{sd}, c_{hu}, and c_+), however due to the similarity of these results, only the results for c_{sd} are shown.

Results are shown for a diffusion problem with $a = 0$ and $b = 1$ in Fig. (1), and an advection–diffusion problem with $a = 1$ and $b = 1$ in Fig. (2). For the diffusion problem, results for polynomial orders $p = 2$ and $p = 3$ are shown. For the advection–diffusion problem, only results for $p = 3$ are shown, as the results for $p = 2$ demonstrate a similar trend.

Several conclusions can be drawn from these experiments. Firstly, the value of κ has an important effect on the accuracy of the scheme, and choosing a large value of κ (defined as $\kappa \gg \kappa_+$) can result in a decrease in the order of accuracy. In contrast, for small and moderate values of κ (defined as $\kappa \lesssim \kappa_+$), the order of accuracy is preserved (in both the solution and its gradient) for all three values of τ.

While κ is the dominant factor affecting the order of accuracy of the 1D VCJH schemes, τ determines when the decrease in accuracy occurs. In particular, decreases in the order of accuracy occur at smaller values of κ for cases with larger values of τ. Smaller values of τ are preferred, and in some cases, choosing a smaller value for τ will raise the order of accuracy of the scheme (as demonstrated by the peaks in the order of accuracy plots in Fig. (1), for the diffusion problem with $\tau = 0$).

More detailed conclusions regarding the affect of τ on convergence rate are difficult to formulate, as the affect of τ appears to depend on the type of advection–diffusion problem. For example, if $\tau = 0$ and $\kappa \gg \kappa_+$ for the pure diffusion problem, the

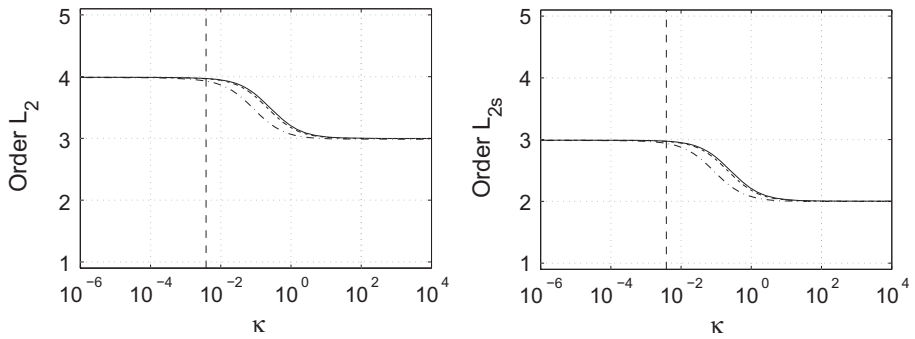

(a) Solution, $p = 3$ (b) Gradient, $p = 3$

Fig. 2. Plots of the order of accuracy with which $E^{(L2)}$ and $E^{(L2s)}$ converge for VCJH schemes with $c = c_{sd}, \beta = 0.5$, and $\kappa \in [10^{-6}, 10^{4}]$, on the model linear advection–diffusion problem with $a = 1, b = 1$, and $p = 3$. Results for $\tau = 0$, 0.1, and 1 are denoted by solid, dashed, and dot-dashed curves, respectively. A vertical dashed line marks the location of $\kappa = \kappa_+ = c_+$.

convergence rate decreases by two orders, whereas if $\tau = 0$ and $\kappa \gg \kappa_+$ for the advection–diffusion problem, the convergence rate decreases by only one order. It is unclear precisely why this difference occurs. However, it is possible that pairing $\tau = 0$ with large values of κ for the pure diffusion problem causes a larger reduction in convergence rate because τ is a penalty parameter that primarily effects the diffusive flux, and is therefore more likely to have a significant impact (either positive or negative) on the pure diffusion problem. Further investigation is needed in order to determine the precise effect of τ.

In summary, these results suggest that the most effective 1D VCJH schemes can be formed by pairing the four values of c (c_{dg}, c_{sd}, c_{hu}, and c_+) with small or moderate values of κ (i.e. $\kappa \lesssim \kappa_+$), and small values of τ (i.e. $\tau \sim 0$).

5.2. Explicit time-step limit results

The stability of explicit time integration schemes such as the RK54 scheme is governed by the Courant–Friedrichs–Lewy (CFL) condition, which places an upper bound on the maximum allowable time-step. Thus, additional experiments were performed in order to determine explicit time-steps limits associated with the VCJH schemes in 1D. For brevity, experiments were only performed using schemes with $c = c_{dg}, c = c_{sd}, c = c_{hu}$, or $c = c_+$ paired with $\kappa = \kappa_{dg}, \kappa = \kappa_{sd}, \kappa = \kappa_{hu}$, or $\kappa = \kappa_+$. Note that these schemes have small or moderate values of κ as recommended in the previous section.

For each scheme, the explicit time-step limit was determined using a bisection method to identify the largest time-step that allowed the solution to remain bounded until $t = 1$. This maximum time step was computed to an accuracy of at least $1e-6$. Tables 2–4 list the dimensionless time-step limit ($\tilde{\Delta t}_{max}$), absolute errors in the solution and solution gradient, and

Table 2
VCJH scheme accuracy properties and explicit time-step limits for model linear advection–diffusion problem in 1D with $a = 0, b = 1$, and $p = 2$. A value of $\beta = 0.5$ was used, and the time-step limit (Δt_{max}) and absolute errors (L_2 and L_{2s} err.) were obtained on the grid with N = 32 elements.

c	κ	$\tau = 0$					$\tau = 0.1$				
		L_2 err.	$O(L_2)$	L_{2s} err.	$O(L_{2s})$	Δt_{max}	L_2 err.	$O(L_2)$	L_{2s} err.	$O(L_{2s})$	Δt_{max}
c_{dg}	κ_{dg}	2.41e−05	3.00	1.26e−03	2.00	1.20e−03	2.41e−05	3.00	1.25e−03	2.00	1.20e−03
	κ_{sd}	3.79e−05	3.00	1.68e−03	2.00	1.58e−03	3.76e−05	3.00	1.67e−03	2.00	1.58e−03
	κ_{hu}	6.03e−05	3.00	2.30e−03	2.00	1.68e−03	5.96e−05	3.00	2.28e−03	2.00	1.68e−03
	κ_+	1.53e−04	3.00	4.84e−03	2.00	1.78e−03	1.49e−04	2.99	4.73e−03	1.99	1.78e−03
c_{sd}	κ_{dg}	2.41e−05	3.00	1.26e−03	2.00	1.58e−03	2.41e−05	3.00	1.25e−03	2.00	1.58e−03
	κ_{sd}	3.79e−05	3.00	1.68e−03	2.00	1.89e−03	3.76e−05	3.00	1.68e−03	2.00	1.89e−03
	κ_{hu}	6.04e−05	3.00	2.30e−03	2.00	2.08e−03	5.97e−05	3.00	2.28e−03	2.00	2.08e−03
	κ_+	1.53e−04	3.00	4.85e−03	2.00	2.30e−03	1.49e−04	2.99	4.74e−03	1.99	2.30e−03
c_{hu}	κ_{dg}	2.42e−05	3.00	1.26e−03	2.00	1.68e−03	2.41e−05	3.00	1.26e−03	2.00	1.67e−03
	κ_{sd}	3.80e−05	3.00	1.69e−03	2.00	2.08e−03	3.78e−05	3.00	1.68e−03	2.00	2.08e−03
	κ_{hu}	6.06e−05	3.00	2.31e−03	2.00	2.34e−03	5.99e−05	3.00	2.29e−03	2.00	2.33e−03
	κ_+	1.54e−04	3.00	4.86e−03	2.00	2.68e−03	1.50e−04	2.99	4.76e−03	1.99	2.67e−03
c_+	κ_{dg}	2.53e−05	3.01	1.27e−03	2.00	1.78e−03	2.52e−05	3.01	1.27e−03	2.00	1.78e−03
	κ_{sd}	3.91e−05	3.01	1.71e−03	2.00	2.30e−03	3.88e−05	3.01	1.70e−03	2.00	2.30e−03
	κ_{hu}	6.18e−05	3.01	2.33e−03	2.00	2.68e−03	6.11e−05	3.00	2.31e−03	2.00	2.67e−03
	κ_+	1.56e−04	3.01	4.93e−03	2.01	3.24e−03	1.52e−04	3.00	4.83e−03	2.00	3.23e−03

Table 3
VCJH scheme accuracy properties and explicit time–step limits for model linear advection–diffusion problem in 1D with, $a = 0, b = 1$, and $p = 3$. A value of $\beta = 0.5$ was used, and the time-step limit (Δt_{max}) and absolute errors (L_2 and L_{2s} err.) were obtained on the grid with N = 32 elements.

c	κ	$\tau = 0$					$\tau = 0.1$				
		L_2 err.	$O(L_2)$	L_{2s} err.	$O(L_{2s})$	Δt_{max}	L_2 err.	$O(L_2)$	L_{2s} err.	$O(L_{2s})$	Δt_{max}
c_{dg}	κ_{dg}	2.91e−07	4.00	2.35e−05	3.00	4.05e−04	2.90e−07	4.00	2.35e−05	3.00	4.05e−04
	κ_{sd}	4.69e−07	4.00	3.45e−05	3.00	4.86e−04	4.67e−07	4.00	3.44e−05	3.00	4.85e−04
	κ_{hu}	6.44e−07	4.00	4.40e−05	3.00	5.05e−04	6.39e−07	4.00	4.37e−05	3.00	5.05e−04
	κ_+	1.18e−06	4.00	7.22e−05	3.00	5.30e−04	1.17e−06	4.00	7.14e−05	3.00	5.30e−04
c_{sd}	κ_{dg}	2.91e−07	4.00	2.35e−05	3.00	4.86e−04	2.90e−07	4.00	2.35e−05	3.00	4.85e−04
	κ_{sd}	4.70e−07	4.00	3.46e−05	3.00	5.77e−04	4.67e−07	4.00	3.44e−05	3.00	5.76e−04
	κ_{hu}	6.45e−07	4.00	4.40e−05	3.00	6.12e−04	6.40e−07	4.00	4.38e−05	3.00	6.11e−04
	κ_+	1.18e−06	4.00	7.22e−05	3.00	6.60e−04	1.17e−06	4.00	7.15e−05	3.00	6.59e−04
c_{hu}	κ_{dg}	2.91e−07	4.00	2.35e−05	3.00	5.05e−04	2.91e−07	4.00	2.35e−05	3.00	5.05e−04
	κ_{sd}	4.70e−07	4.00	3.46e−05	3.00	6.12e−04	4.68e−07	4.00	3.45e−05	3.00	6.11e−04
	κ_{hu}	6.45e−07	4.00	4.40e−05	3.00	6.55e−04	6.40e−07	4.00	4.38e−05	3.00	6.54e−04
	κ_+	1.18e−06	4.00	7.23e−05	3.00	7.16e−04	1.17e−06	4.00	7.15e−05	3.00	7.14e−04
c_+	κ_{dg}	2.93e−07	4.00	2.36e−05	3.00	5.30e−04	2.92e−07	4.00	2.35e−05	3.00	5.30e−04
	κ_{sd}	4.72e−07	4.00	3.47e−05	3.00	6.60e−04	4.70e−07	4.00	3.45e−05	3.00	6.59e−04
	κ_{hu}	6.48e−07	4.00	4.42e−05	3.00	7.15e−04	6.43e−07	4.00	4.39e−05	3.00	7.14e−04
	κ_+	1.19e−06	4.00	7.25e−05	3.00	7.97e−04	1.17e−06	4.00	7.17e−05	3.00	7.96e−04

Table 4
VCJH scheme accuracy properties and explicit time-step limits for model linear advection–diffusion problem in 1D with, $a = 1, b = 1$, and $p = 3$. A value of $\beta = 0.5$ was used, and the time-step limit (Δt_{max}) and absolute errors (L_2 and L_{2s} err.) were obtained on the grid with N = 32 elements.

c	κ	$\tau = 0$					$\tau = 0.1$				
		L_2 err.	$O(L_2)$	L_{2s} err.	$O(L_{2s})$	Δt_{max}	L_2 err.	$O(L_2)$	L_{2s} err.	$O(L_{2s})$	Δt_{max}
c_{dg}	κ_{dg}	2.86e−07	3.99	2.31e−05	2.99	4.02e−04	2.86e−07	3.99	2.31e−05	2.99	4.01e−04
	κ_{sd}	4.53e−07	3.99	3.36e−05	2.99	4.84e−04	4.51e−07	3.99	3.35e−05	2.99	4.83e−04
	κ_{hu}	6.15e−07	3.98	4.25e−05	2.99	5.03e−04	6.11e−07	3.98	4.22e−05	2.99	5.03e−04
	κ_+	1.10e−06	3.97	6.81e−05	2.98	5.28e−04	1.09e−06	3.97	6.74e−05	2.98	5.28e−04
c_{sd}	κ_{dg}	2.82e−07	3.99	2.29e−05	2.99	4.83e−04	2.82e−07	3.99	2.29e−05	2.99	4.83e−04
	κ_{sd}	4.46e−07	3.98	3.32e−05	2.99	5.73e−04	4.44e−07	3.98	3.31e−05	2.98	5.72e−04
	κ_{hu}	6.06e−07	3.98	4.20e−05	2.98	6.08e−04	6.02e−07	3.98	4.17e−05	2.98	6.08e−04
	κ_+	1.09e−06	3.97	6.73e−05	2.97	6.56e−04	1.07e−06	3.97	6.66e−05	2.97	6.55e−04
c_{hu}	κ_{dg}	2.80e−07	3.99	2.27e−05	2.99	5.02e−04	2.79e−07	3.99	2.27e−05	2.99	5.02e−04
	κ_{sd}	4.40e−07	3.98	3.29e−05	2.98	6.08e−04	4.38e−07	3.98	3.28e−05	2.98	6.07e−04
	κ_{hu}	5.99e−07	3.97	4.16e−05	2.98	6.51e−04	5.95e−07	3.97	4.14e−05	2.98	6.50e−04
	κ_+	1.08e−06	3.97	6.67e−05	2.97	7.11e−04	1.06e−06	3.96	6.61e−05	2.97	7.10e−04
c_+	κ_{dg}	2.74e−07	3.98	2.23e−05	2.98	5.27e−04	2.73e−07	3.98	2.22e−05	2.98	5.26e−04
	κ_{sd}	4.26e−07	3.96	3.21e−05	2.97	6.54e−04	4.24e−07	3.96	3.20e−05	2.97	6.53e−04
	κ_{hu}	5.80e−07	3.96	4.06e−05	2.97	7.10e−04	5.76e−07	3.96	4.03e−05	2.97	7.09e−04
	κ_+	1.05e−06	3.96	6.51e−05	2.96	7.90e−04	1.03e−06	3.95	6.45e−05	2.96	7.89e−04

order of accuracy for each scheme. The time-step limit and absolute errors were obtained on the grid with N = 32 elements. Results are presented for a value of $\beta = 0.5$, and two values of $\tau : \tau = 0$ and 0.1. Tables (2) and (3) present these results for the diffusion problem (with $p = 2$ and $p = 3$), and Table (4) presents these results for the advection–diffusion problem (with p = 3). The results for the diffusion problem and the advection–diffusion problem are similar, and thus limited results (only the results for $p = 3$) are shown for the advection–diffusion problem.

5.3. Summary of one-dimensional linear numerical experiments

For the diffusion problem, larger values of c and κ yield larger values for the maximum time-step. Table (2) shows that for $p = 2, \tau = 0, c = c_+$, and $\kappa = \kappa_+$, the maximum time-step is 2.7 times that of the maximum allowable time-step for a collocation-based nodal DG scheme (with $c = 0$ and $\kappa = 0$). Time-step improvements are also obtained for advection–diffusion problems. In all cases, values of $c > c_{dg}$ paired with values of $\kappa > \kappa_{dg}$ consistently produce larger maximum time-steps (relative to a collocation-based nodal DG scheme). However, it should be noted that raising c and κ also increases absolute errors in both the solution and the solution gradient. Consequently, for schemes with $c > c_{dg}$ and $\kappa > \kappa_{dg}$, finer meshes would be required to achieve error levels associated with a collocation-based nodal DG scheme. These finer meshes would act to reduce the maximum allowable time-step, potentially offsetting any increases associated with raising c and κ. Further studies

are required to determine whether in practice, under the constraint of a fixed error tolerance, increasing c and κ has an overall benefit in terms of increasing the maximum allowable time-step.

6. Two-dimensional nonlinear numerical experiments

In this section, numerical experiments were performed using the 2D Navier–Stokes equations to verify if the findings of the previous section also hold for nonlinear problems in multiple dimensions. In 2D, the Navier–Stokes equations take the form

$$\frac{\partial U}{\partial t} + \nabla \cdot \mathbf{F}_{inv}(U) - \nabla \cdot \mathbf{F}_{visc}(U, \nabla U) = 0, \tag{79}$$

where U represents the conservative variables, and $\mathbf{F}_{inv} = (f_{inv}, g_{inv})$ and $\mathbf{F}_{visc} = (f_{visc}, g_{visc})$ represent the inviscid and viscous flux vectors, respectively. The conservative variables and the x and y components of the inviscid flux vector can be written as follows

$$U = \begin{Bmatrix} \rho \\ \rho u \\ \rho v \\ E \end{Bmatrix}, \quad f_{inv} = \begin{Bmatrix} \rho u \\ \rho u^2 + p \\ \rho u v \\ u(E+p) \end{Bmatrix}, \quad g_{inv} = \begin{Bmatrix} \rho v \\ \rho u v \\ \rho v^2 + p \\ v(E+p) \end{Bmatrix}, \tag{80}$$

where $\rho = \rho(x,y,t)$ is the density, $u = u(x,y,t)$ and $v = v(x,y,t)$ are the x and y components of velocity, $p = p(x,y,t)$ is the pressure, $E = p/(\gamma - 1) + (1/2)\rho(u^2 + v^2)$ is the total energy, and γ is the ratio of specific heats of the fluid. The x and y components of the viscous flux vector can be written as

$$f_{visc} = \mu \begin{Bmatrix} 0 \\ 2u_x + \lambda(u_x + v_y) \\ v_x + u_y \\ u[2u_x + \lambda(u_x + v_y)] + v(v_x + u_y) + \frac{C_p}{P_r} T_x \end{Bmatrix},$$

$$g_{visc} = \mu \begin{Bmatrix} 0 \\ v_x + u_y \\ 2v_y + \lambda(u_x + v_y) \\ v[2v_y + \lambda(u_x + v_y)] + u(v_x + u_y) + \frac{C_p}{P_r} T_y \end{Bmatrix}, \tag{81}$$

where μ is the dynamic viscosity, λ is the bulk viscosity coefficient (equal to $-2/3$ by Stoke's hypothesis), C_p is the specific heat capacity at constant pressure, P_r is the Prandtl number, $T = p/(\rho R)$ is the temperature, and R is the gas constant. In each of the flux components above, the subscripts x and y represent first derivatives with respect to x and y (i.e. $u_x = \frac{\partial u}{\partial x}$). These first derivatives in the flux components result in second derivatives in the governing equation (Eq. (79)). The second derivatives can be eliminated by rewriting Eq. (79) as a first-order system

$$\frac{\partial U}{\partial t} + \nabla \cdot \mathbf{F}_{inv}(U) - \nabla \cdot \mathbf{F}_{visc}(U, Q) = 0, \tag{82}$$

$$Q - \nabla U = 0 \tag{83}$$

where Q is the auxiliary state vector. Couette flow is a well-known analytical solution to Eq. (79) (and by extension to Eqs. (82) and (83)). Consider the case where two walls (of infinite extent in the x and z directions) are separated by a distance H in the y direction. The lower wall is stationary and has a temperature of T_w, while the upper wall is moving with speed U_w in the x direction and has a temperature of ηT_w. If $\mu = \text{const}$, the pressure $p = \text{const}$, and there is an analytical solution for the total energy E which takes the form

$$E = p\left[\frac{1}{\gamma - 1} + \frac{\frac{U_w^2}{2R}\left(\frac{y}{H}\right)^2}{T_w + \left(\frac{y}{H}\right)(\eta - 1)T_w + \frac{P_r U_w^2}{2C_p}\left(\frac{y}{H}\right)\left[1 - \left(\frac{y}{H}\right)\right]}\right]. \tag{84}$$

Approximate solutions to this problem were obtained using VCJH schemes in conjunction with the RK54 scheme for time marching, the Rusanov approach for computing the inviscid numerical fluxes and the LDG approach for computing the viscous numerical fluxes. The 1D approach was extended to 2D on quadrilateral elements using a tensor product formulation consistent with the approach used in [14,15,27].

Solutions were obtained on the rectangular domain $[-1, 1] \times [0, 1]$ using regular quadrilateral grids with $2\tilde{N} \times \tilde{N}$ elements. The initial condition for each simulation was a uniform flow of air ($Pr = 0.72,\ \gamma = 1.4$) with $u = U_w$ and $v = 0$. The flow was constrained on the left and right by periodic boundary conditions, from below by an isothermal wall boundary condition (with $u = 0$ and $T_w = 300\,\text{K}$), and from above by a moving isothermal wall boundary condition (with $u = U_w$ and

$\eta = 1.05$). During the simulations, the pressure at the moving wall was fixed ($p = \text{const}$). The value of U_w was chosen such that the Mach number at the moving wall was $M = 0.2$, and the Reynolds number (based on $H = 1.0$) was 200. Under these conditions, each simulation was marched forward in time until the residual reached machine zero.

6.1. Accuracy and explicit time-step results

Table 5–7 contain accuracy and explicit time-step results for several VCJH schemes formed by pairing: (1) c_{dg} and κ_{dg}, (2) c_{sd} and κ_{sd}, (3) c_{hu} and κ_{hu}, and finally (4) c_+ and κ_+. Each scheme was run with polynomial orders $p = 2$ and $p = 3$, a value of β equal to 0.5 and values of $\tau = 0$ and $\tau = 0.1$. In each case, orders of accuracy and absolute measurements of the error were obtained using L2 norms and seminorms of errors in the total energy E and its gradient ∇E. Explicit time-step limits were obtained on a grid with $\tilde{N} = 8$.

Table 5
Accuracy of VCJH schemes for the Couette flow problem: $p = 2$. The inviscid numerical flux was computed using a Rusanov flux and the viscous numerical flux was computed using a LDG flux with $\beta = 0.5$.

c, κ	Grid	$\tau = 0$				$\tau = 0.1$			
		L_2 err.	$O(L_2)$	L_{2s} err.	$O(L_{2s})$	L_2 err.	$O(L_2)$	L_{2s} err.	$O(L_{2s})$
c_{dg}, κ_{dg}	$\tilde{N} = 2$	7.39e−05		1.83e−03		7.33e−05		1.83e−03	
	$\tilde{N} = 4$	8.93e−06	3.05	4.56e−04	2.01	8.97e−06	3.03	4.56e−04	2.01
	$\tilde{N} = 8$	1.11e−06	3.01	1.13e−04	2.01	1.12e−06	3.00	1.13e−04	2.01
	$\tilde{N} = 16$	1.41e−07	2.98	2.80e−05	2.01	1.40e−07	3.01	2.80e−05	2.01
c_{sd}, κ_{sd}	$\tilde{N} = 2$	7.41e−05		1.83e−03		7.33e−05		1.83e−03	
	$\tilde{N} = 4$	8.92e−06	3.05	4.56e−04	2.01	8.95e−06	3.04	4.56e−04	2.01
	$\tilde{N} = 8$	1.11e−06	3.01	1.13e−04	2.01	1.11e−06	3.01	1.13e−04	2.01
	$\tilde{N} = 16$	1.40e−07	2.99	2.80e−05	2.01	1.39e−07	3.00	2.80e−05	2.01
c_{hu}, κ_{hu}	$\tilde{N} = 2$	7.41e−05		1.83e−03		7.34e−05		1.83e−03	
	$\tilde{N} = 4$	8.92e−06	3.05	4.56e−04	2.01	8.94e−06	3.04	4.56e−04	2.01
	$\tilde{N} = 8$	1.11e−06	3.01	1.13e−04	2.01	1.11e−06	3.01	1.13e−04	2.01
	$\tilde{N} = 16$	1.39e−07	2.99	2.81e−05	2.01	1.39e−07	3.00	2.80e−05	2.01
c_+, κ_+	$\tilde{N} = 2$	7.42e−05		1.83e−03		7.34e−05		1.83e−03	
	$\tilde{N} = 4$	8.92e−06	3.06	4.56e−04	2.01	8.93e−06	3.04	4.56e−04	2.01
	$\tilde{N} = 8$	1.10e−06	3.01	1.13e−04	2.01	1.11e−06	3.01	1.13e−04	2.01
	$\tilde{N} = 16$	1.39e−07	2.99	2.81e−05	2.01	1.39e−07	3.00	2.80e−05	2.01

Table 6
Accuracy of VCJH schemes for the Couette flow problem: $p = 3$. The inviscid numerical flux was computed using a Rusanov flux and the viscous numerical flux was computed using a LDG flux with $\beta = 0.5$.

c, κ	Grid	$\tau = 0$				$\tau = 0.1$			
		L_2 err.	$O(L_2)$	L_{2s} err.	$O(L_{2s})$	L_2 err.	$O(L_2)$	L_{2s} err.	$O(L_{2s})$
c_{dg}, κ_{dg}	$\tilde{N} = 1$	2.72e−05		4.85e−04		2.69e−05		4.85e−04	
	$\tilde{N} = 2$	1.55e−06	4.13	5.96e−05	3.02	1.56e−06	4.11	5.96e−05	3.02
	$\tilde{N} = 4$	9.68e−08	4.01	7.44e−06	3.00	9.76e−08	4.00	7.44e−06	3.00
	$\tilde{N} = 8$	6.07e−09	3.99	9.30e−07	3.00	6.13e−09	3.99	9.30e−07	3.00
c_{sd}, κ_{sd}	$\tilde{N} = 1$	2.72e−05		4.85e−04		2.69e−05		4.85e−04	
	$\tilde{N} = 2$	1.55e−06	4.13	5.96e−05	3.02	1.56e−06	4.11	5.96e−05	3.02
	$\tilde{N} = 4$	9.67e−08	4.01	7.44e−06	3.00	9.71e−08	4.01	7.44e−06	3.00
	$\tilde{N} = 8$	6.06e−09	3.99	9.30e−07	3.00	6.08e−09	4.00	9.30e−07	3.00
c_{hu}, κ_{hu}	$\tilde{N} = 1$	2.72e−05		4.85e−04		2.69e−05		4.85e−04	
	$\tilde{N} = 2$	1.55e−06	4.13	5.95e−05	3.02	1.56e−06	4.11	5.96e−05	3.02
	$\tilde{N} = 4$	9.67e−08	4.01	7.44e−06	3.00	9.70e−08	4.01	7.44e−06	3.00
	$\tilde{N} = 8$	6.07e−09	3.99	9.30e−07	3.00	6.08e−09	4.00	9.30e−07	3.00
c_+, κ_+	$\tilde{N} = 1$	2.72e−05		4.85e−04		2.69e−05		4.85e−04	
	$\tilde{N} = 2$	1.55e−06	4.13	5.95e−05	3.02	1.56e−06	4.11	5.96e−05	3.02
	$\tilde{N} = 4$	9.68e−08	4.00	7.44e−06	3.00	9.69e−08	4.01	7.44e−06	3.00
	$\tilde{N} = 8$	6.09e−09	3.99	9.29e−07	3.00	6.07e−09	4.00	9.30e−07	3.00

Table 7
Time–step limits (Δt_{max}) of VCJH schemes on the grid with $\tilde{N} = 8$ for the Couette flow problem: $p = 2$ and 3. The inviscid numerical flux was computed using a Rusanov flux and the viscous numerical flux was computed using a LDG flux with $\beta = 0.5$

	$p = 2$		$p = 3$	
	$\tau = 0$	$\tau = 0.1$	$\tau = 0$	$\tau = 0.1$
c_{dg}, κ_{dg}	3.79e−03	3.67e−03	2.04e−03	1.99e−03
c_{sd}, κ_{sd}	5.93e−03	5.75e−03	3.09e−03	3.00e−03
c_{hu}, κ_{hu}	7.84e−03	7.59e−03	3.55e−03	3.44e−03
c_{+}, κ_{+}	8.10e−03	7.84e−03	3.67e−03	3.56e−03

The results indicate that, as c and κ increase, the time-step limit increases. This trend, which was originally observed for the 1D linear problems, holds in the context of this 2D nonlinear problem. For $p = 2$ and $\tau = 0$, Table (7) shows that the scheme with $c = c_{dg}$ and $\kappa = \kappa_{dg}$ has a time-step limit of 3.79e−03, while the scheme with $c = c_{+}$ and $\kappa = \kappa_{+}$ has a time-step limit of 8.10e−03.

Finally, the results indicate that increasing c and κ (and thus increasing the time-step limit) has a negligible effect on the absolute error of the scheme. This is in contrast to the 1D, linear results, where increasing c and κ caused an increase in the absolute error, and in some cases, a slight decrease in the order of accuracy. For the Couette flow experiments, the error is not significantly affected by c and κ, and the expected order of accuracy is achieved for all schemes, for both values of τ ($\tau = 0$ and $\tau = 0.1$).

7. Conclusions

A FR formulation for solving advection–diffusion problems has been presented which utilizes both flux and solution correction functions. Using an energy method, it has been shown that if both these correction functions are of VCJH type (previously identified in the context of pure advection problems), then the resulting FR scheme will be stable for linear advection–diffusion problems, for all orders of accuracy. Consequently, the paper identifies, for the first time, a range of provably stable FR schemes for advection–diffusion problems, for all orders of accuracy. 1D linear experiments show that certain VCJH schemes for advection–diffusion problems possess significantly higher explicit time-step limits than DG schemes, while still maintaining the expected order of accuracy. Two-dimensional numerical experiments using the Navier–Stokes equations confirm that such properties extend to a tensor product formulation with nonlinear fluxes.

Acknowledgments

The authors thank the National Science Foundation Graduate Research Fellowship Program, the Natural Sciences and Engineering Research Council of Canada, the Fonds Québécois de Recherche sur la Nature et les Technologies, the Stanford Graduate Fellowships program, the National Science Foundation (grants 0708071 and 0915006), the Air Force Office of Scientific Research (grants FA9550-07-1-0195 and FA9550-10-1-0418) and NVIDIA for supporting this work.

References

[1] P.E. Vincent, A. Jameson, Facilitating the adoption of unstructured high-order methods amongst a wider community of fluid dynamicists, Math. Model. Nat. Phenom. 6 (2011) 97–140.
[2] J. Hesthaven, T. Warburton, Nodal Discontinuous Galerkin methods: Algorithms, Analysis, and Applications, Springer Verlag, 2007.
[3] C. Shu, High-order finite difference and finite volume WENO schemes and discontinuous Galerkin methods for CFD, Int. J. Comput. Fluid Dyn. 17 (2003) 107–118.
[4] W. Reed, T. Hill, Triangular mesh methods for the neutron transport equation, Los Alamos, Report LA-UR-73-479, 1973.
[5] F. Bassi, S. Rebay, High-order accurate discontinuous finite element solution of the 2D Euler equations, J. Comput. Phys. 138 (1997) 251–285.
[6] F. Bassi, S. Rebay, A high-order accurate discontinuous finite element method for the numerical solution of the compressible Navier–Stokes equations, J. Comput. Phys. 131 (1997) 267–279.
[7] C. Baumann, J. Oden, A discontinuous hp finite element method for the Euler and Navier–Stokes equations, Int. J. Numer. Methods Fluids 31 (1999) 79–95.
[8] D.A. Kopriva, J.H. Kolias, A conservative staggered-grid Chebyshev multidomain method for compressible flows, J. Comput. Phys. 125 (1996) 244–261.
[9] Y. Liu, M. Vinokur, Z.J. Wang, Spectral difference method for unstructured grids I: basic formulation, J. Comput. Phys. 216 (2006) 780–801.
[10] Z. Wang, Y. Liu, G. May, A. Jameson, Spectral difference method for unstructured grids II: extension to the Euler equations, J. Sci. Comput. 32 (2007) 45–71.
[11] C. Liang, A. Jameson, Z. Wang, Spectral difference method for compressible flow on unstructured grids with mixed elements, J. Comput. Phys. 228 (2009) 2847–2858.
[12] P. Castonguay, C. Liang, A. Jameson, Simulation of transitional flow over airfoils using the spectral difference method, in: AIAA P. (2010), 40th AIAA Fluid Dynamics Conference, Chicago, IL, 28 Jun – 1 Jul, 2010.
[13] K. Ou, P. Castonguay, A. Jameson, 3D flapping wing simulation with high order spectral difference method on deformable mesh, in: AIAA P. (2011), 49th AIAA Aerospace Sciences Meeting, Orlando, FL, Jan 4–7, 2011.
[14] H. Huynh, A flux reconstruction approach to high-order schemes including discontinuous Galerkin methods, in: AIAA P. (2007). 18th AIAA Computational Fluid Dynamics Conference, Miami, FL, Jun 25–28, 2007.
[15] H. Huynh, A reconstruction approach to high-order schemes including discontinuous Galerkin for diffusion, in: AIAA P. (2009). 47th AIAA Aerospace Sciences Meeting, Orlando, FL, Jan 5–8, 2009.

[16] H. Huynh, High-order methods including discontinuous Galerkin by reconstructions on triangular meshes, in: AIAA P. (2011). 49th AIAA Aerospace Sciences Meeting, Orlando, FL, Jan 4–7, 2011.
[17] Z.J. Wang, H. Gao, A high-order lifting collocation penalty formulation for the Navier-Stokes equations on 2D mixed grids, in: AIAA P. (2009). 19th AIAA Computational Fluid Dynamics, San Antonio, TX, June 22–25, 2009.
[18] Z. Wang, H. Gao, A unifying lifting collocation penalty formulation including the discontinuous Galerkin, spectral volume/difference methods for conservation laws on mixed grids, J. Comput. Phys. 228 (2009) 8161–8186.
[19] Z. Wang, H. Gao, A unifying lifting collocation penalty formulation for the Euler equations on mixed grids, in: AIAA P. (2009) 47th AIAA Aerospace Sciences Meeting Orlando FL, Jan 5–8, 2009.
[20] T. Haga, H. Gao, Z. Wang, A high-order unifying discontinuous formulation for 3D mixed grids, in: AIAA P. (2010). 48th AIAA Aerospace Sciences Meeting, Orlando, FL, Jan 4–7, 2010.
[21] M. Yu, Z. Wang, On the connection between the correction and weighting functions in the correction procedure via reconstruction method, J. Sci. Comput. (2012), http://dx.doi.org/10.1007/s10915-012-9618-3.
[22] H. Gao, Z. Wang, H. Huynh, Differential formulation of discontinuous galerkin and related methods for the Navier–Stokes equations, Communications in Computational Physics, in press (2013).
[23] Z.J. Wang, Adaptive High-order Methods in Computational Fluid Dynamics, vol. 2, World Scientific Publishing Company, 2011.
[24] H. Huynh, High-order methods including discontinuous galerkin by reconstructions on triangular meshes, AIAA Paper 44, 2011.
[25] T. Haga, H. Gao, Z. Wang, A high-order unifying discontinuous formulation for the Navier–Stokes equations on 3D mixed grids, Math. Model. Nat. Phenom. 6 (2011) 28–56.
[26] A. Jameson, A proof of the stability of the spectral difference method for all orders of accuracy, J. Sci. Comput. 45 (2010) 348–358.
[27] P.E. Vincent, P. Castonguay, A. Jameson, Insights from von Neumann analysis of high-order flux reconstruction schemes, J. Comput. Phys. 230 (2011) 8134–8154.
[28] P.E. Vincent, P. Castonguay, A. Jameson, A new class of high-order energy stable flux reconstruction schemes, J. Sci. Comput. 47 (2011) 50–72.
[29] D.M. Williams, P. Castonguay, P.E. Vincent, A. Jameson, An extension of energy stable flux reconstruction to unsteady, non-linear, viscous problems on mixed grids, in: AIAA P. (2011). 20th AIAA Computational Fluid Dynamics Conference, Honolulu, Hawaii, June 27–30, 2011.
[30] B. Cockburn, C. Shu, The local discontinuous Galerkin method for time-dependent convection–diffusion systems, SIAM J. Numer. Anal. 35 (1998) 2440–2463.
[31] J. Peraire, P. Persson, The compact discontinuous Galerkin (CDG) method for elliptic problems, SIAM J. Sci. Comput. 30 (2009) 1806–1824.
[32] D. Arnold, An interior penalty finite element method with discontinuous elements, SIAM J. Numer. Anal. 19 (1982) 742–760.
[33] F. Bassi, S. Rebay, G. Mariotti, S. Pedinotti, M. Savini, A high-order accurate discontinuous finite element method for inviscid and viscous turbomachinery flows, in: R. Decuypere, G. Dibelius (Eds.) 2nd European Conference on Turbomachinery Fluid Dynamics and Thermodynamics (Antwerpen, Belgium), Technologisch Instituut, pp. 99–108.
[34] P.L. Roe, Approximate riemann solvers, parameter vectors and difference schemes, J. Comput. Phys. 43 (1981) 357–372.
[35] V.V. Rusanov, Calculation of interaction of non-steady shock waves with obstacles, J. Comput. Math Phys. USSR 1 (1961) 261–279.
[36] P. Castonguay, High-Order Energy Stable Flux Reconstruction Schemes for Fluid Flow Simulations on Unstructured Grids, Ph.D. thesis, Stanford University, 2012.
[37] M.H. Carpenter, C. Kennedy, Fourth-order 2N-storage Runge–Kutta schemes, Technical Report TM 109112, NASA, NASA Langley Research Center, 1994.
[38] P. Castillo, B. Cockburn, I. Perugia, D. Schotzau, An a priori error analysis of the local discontinuous Galerkin method for elliptic problems, SIAM J. Numer. Anal. 38 (2001) 1676–1706.
[39] D. Arnold, F. Brezzi, B. Cockburn, L. Marini, Unified analysis of discontinuous Galerkin methods for elliptic problems, SIAM J. Numer. Anal. (2002) 1749–1779.